

# Mechanical strain sensing implicated in cell shape recovery in *Escherichia coli*

Felix Wong<sup>1†</sup>, Lars D. Renner<sup>2,3\*†</sup>, Gizem Özbaykal<sup>4</sup>, Jayson Paulose<sup>5</sup>, Douglas B. Weibel<sup>3,6</sup>, Sven van Teeffelen<sup>4</sup> and Ariel Amir<sup>1\*</sup>

**The shapes of most bacteria are imparted by the structures of their peptidoglycan cell walls, which are determined by many dynamic processes that can be described on various length scales ranging from short-range glycan insertions to cellular-scale elasticity<sup>1–11</sup>. Understanding the mechanisms that maintain stable, rod-like morphologies in certain bacteria has proved to be challenging due to an incomplete understanding of the feedback between growth and the elastic and geometric properties of the cell wall<sup>3,4,12–14</sup>. Here, we probe the effects of mechanical strain on cell shape by modelling the mechanical strains caused by bending and differential growth of the cell wall. We show that the spatial coupling of growth to regions of high mechanical strain can explain the plastic response of cells to bending<sup>4</sup> and quantitatively predict the rate at which bent cells straighten. By growing filamentous *Escherichia coli* cells in doughnut-shaped microchambers, we find that the cells recovered their straight, native rod-shaped morphologies when released from captivity at a rate consistent with the theoretical prediction. We then measure the localization of MreB, an actin homologue crucial to cell wall synthesis, inside confinement and during the straightening process, and find that it cannot explain the plastic response to bending or the observed straightening rate. Our results implicate mechanical strain sensing, implemented by components of the elongosome yet to be fully characterized, as an important component of robust shape regulation in *E. coli*.**

Cell shape, which in many types of bacteria is determined by a mechanically rigid peptidoglycan (PG) cell wall, is crucial for bacterial motility, proliferation, adhesion and survival<sup>1–3</sup>. Rod-like bacteria maintain their shapes at a fixed diameter with extraordinary precision during growth, and elongate by the action of the peptidoglycan elongation machinery (PGEM), a multi-enzyme complex consisting of penicillin-binding proteins (PBPs) and conserved membrane proteins (MreC, MreD, RodA, RodZ and other shape, elongation, division, sporulation (SEDS) family proteins)<sup>5,6,15,16</sup>. Recent experimental studies have led to a qualitative description of cell wall growth on a molecular level: the PGEM interacts with the actin homologue MreB to direct the local, circumferential insertion of new glycan strands into the existing PG structure. Although the general roles of PGEM enzymes in cell wall elongation are well studied<sup>5–9,17</sup>, the feedback mechanism between cell shape—as determined by the geometric and elastic properties of the cell wall—and PGEM-related subcellular components is not understood. It is unclear whether the mechanisms needed to maintain robust cellular morphology detect cellular geometry<sup>12,18</sup> or mechanical stresses<sup>3,4,13,14</sup>.

Recent progress has been made towards understanding the regulatory mechanisms controlling rod-like cell shape by mechanically perturbing PG, which can be modelled as a partially ordered elastic sheet subject to both plastic and elastic deformations<sup>3,4,14,19</sup>. *Escherichia coli* cells adapt their growing morphologies to confining environments<sup>20,21</sup> or applied hydrodynamic drag forces<sup>4,19</sup> by elongating in a manner that results in bending. In several experiments, *E. coli* cells have recovered their straight, native rod-like morphologies upon release from confining environments<sup>4,19–21</sup> or disruption of an induced crescentin structure<sup>22</sup> after sufficient growth. This striking robustness has led to three prevalent theories of shape regulation: (1) a large processivity—the mean number of subunits incorporated into a glycan strand from initiation to termination of the elongation step—provides a built-in mechanism for straightening<sup>23</sup>; (2) PGEM-related molecules such as MreB localize, according to cell wall geometry, to regions of negative Gaussian curvature<sup>12,18</sup>; and (3) new glycan strands are preferentially inserted at regions of high mechanical stress in a manner that straightens the cell<sup>4,13,22,23</sup>.

By itself, the processivity of PG synthesis cannot explain cell straightening. Although processive glycan insertions into the PG mesh have been shown to yield an exponential decay of curvature<sup>23</sup>, an exponential increase in length due to growth counteracts the straightening and leads to a self-similar, scale-invariant shape, even in the limit of infinite processivity<sup>3,24</sup>. The local curvature of a growing, self-similar crescent-shaped cell decays, but in the absence of cell division the cell is always bent and not truly rod-like (Fig. 1a). Similarly, the possible curvature-sensing abilities of PGEM-related subcellular components have been interpreted as a geometry-based feedback mechanism for shape regulation<sup>12,18</sup>. Such mechanisms would allow the cell to preferentially grow at regions of negative Gaussian curvature and thus result in straightening. However, such a mechanism cannot explain experiments subjecting *E. coli* and *Bacillus subtilis* cells to hydrodynamic drag<sup>4,19</sup>. If the local growth of PG were biased towards regions of negative Gaussian curvature, then more growth would occur along the edge facing away from the flow. Upon extinguishing the flow, the cells would bend in the direction opposite the flow because of the stored, anisotropic growth (Fig. 1b). It was observed, on the contrary, that the equilibrated, bent conformations were in the same direction as the flow.

We therefore hypothesized that a mechanical strain-based, as opposed to geometry-based, pattern of preferential PG elongation could reconcile the aforementioned observations and robustly straighten a cell. The elastic quantity that we examine is the areal

<sup>1</sup>School of Engineering and Applied Sciences, Harvard University, Cambridge, Massachusetts 02138, USA. <sup>2</sup>Leibniz Institute of Polymer Research and the Max Bergmann Center of Biomaterials, 01069 Dresden, Germany. <sup>3</sup>Department of Biochemistry, University of Wisconsin-Madison, Madison, Wisconsin 53706, USA. <sup>4</sup>Department of Microbiology, Institut Pasteur, 75724 Paris, France. <sup>5</sup>Departments of Physics and Integrative Biology, University of California, Berkeley, California 94720, USA. <sup>6</sup>Department of Biomedical Engineering, University of Wisconsin-Madison, Madison, Wisconsin 53706, USA. †These authors contributed equally to this work. \*e-mail: [renner@ipfdd.de](mailto:renner@ipfdd.de); [arielamir@seas.harvard.edu](mailto:arielamir@seas.harvard.edu)

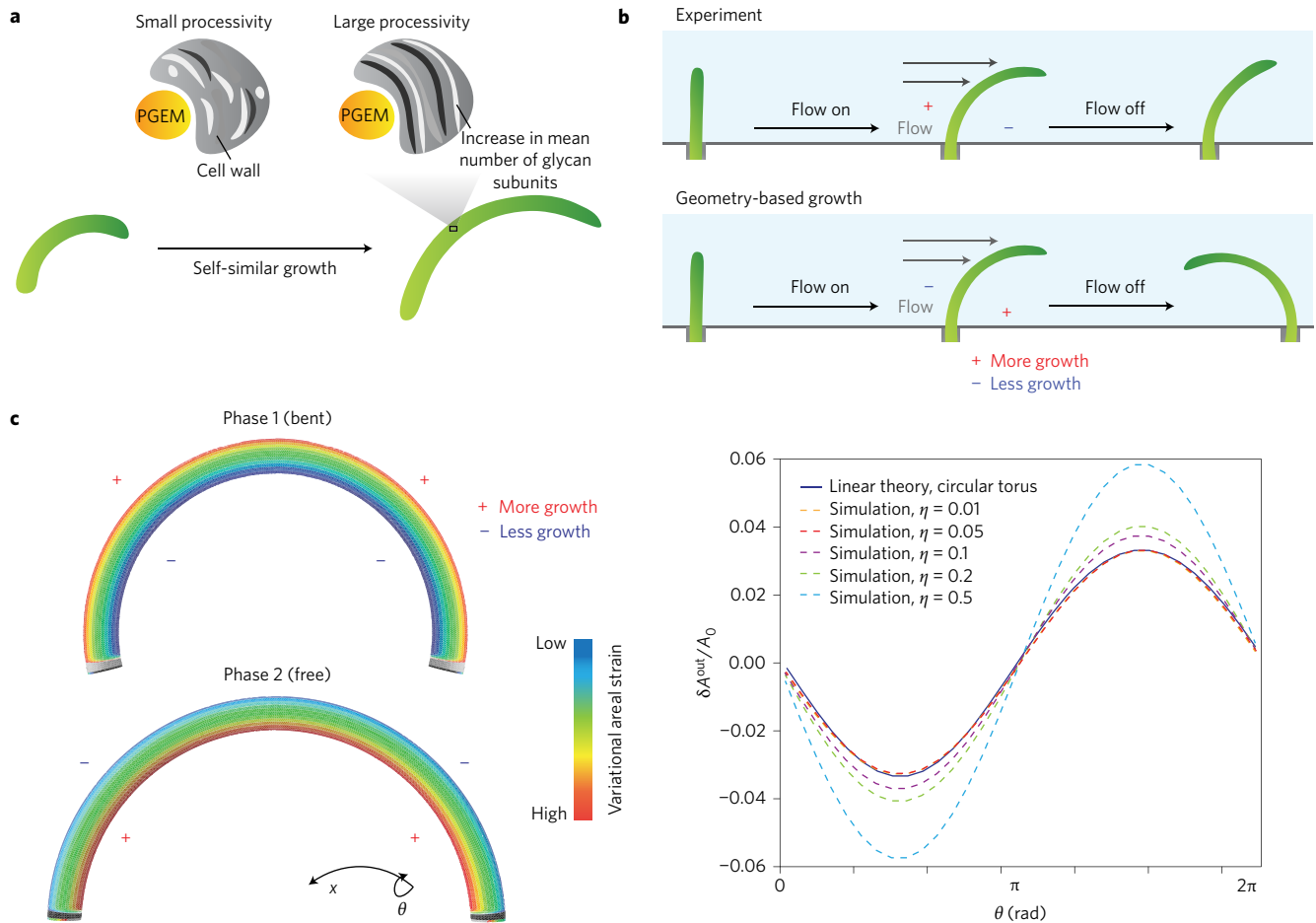


**Figure 1 | Three theories for cellular shape regulation.** **a**, The processivity of glycan insertions provides a robust, built-in mechanism for curvature decay, but even in the infinitely processive limit a cell remains self-similar. **b**, A geometry-dependent growth mechanism predicts an oppositely bent shape once an applied hydrodynamic drag force is extinguished, which was not observed in previous experiments. **c**, A mechanical-strain-dependent growth rate can explain both the elastic snapback shown in **b** and straightening, and the straightening rate can be quantitatively predicted. Left: simulated equilibrium configurations of a bent cylinder (top) and a toroidal shell (bottom) subject to an internal pressure, which respectively describe the cell states under a bending force (phase 1) and in the absence of a bending force (phase 2). The mesh, processed using finite-element software, is coloured by the variational areal strain  $\delta A$ . Like the differential growth,  $\delta A$  flips sign between the two phases.  $x$  and  $\theta$  denote surface coordinates on the cell. Right: simulated, normalized variational areal strain for a differential growth parameter  $c = 0.1$  and varying values of dimensionless pressure  $\eta$  are plotted against the azimuthal angle  $\theta$ , along with the linear theory prediction, for a phase 2 cell. Values of  $\eta$  are calculated using the radii of deformed states. The Poisson ratio is taken to be  $\nu = 0.3$  and the remaining simulation parameters are detailed in the Supplementary Methods.

strain, which measures the local stretching of PG and is defined in terms of the axial and circumferential components of the strain tensor,  $u_{xx}$  and  $u_{yy}$ , respectively, as  $A = (1 + u_{xx})(1 + u_{yy}) - 1$ . A molecular mechanism that couples growth to PG pore size, for instance, may sense areal strain. As we discuss below, the key assumptions of our model are (1) the elastic properties of the cell wall are unaltered by growth and (2) the number of glycan strand initiations per unit area is modulated by areal strain. With these assumptions, we will show that strain-dependent PG elongation is quantitatively consistent with both the earlier flow-based experiments<sup>4</sup> and experimental measurements of the straightening rate.

To test our hypothesis of strain-dependent PG elongation, we designed an experiment consisting of two phases. In phase 1, filamentous cells are confined and uniformly bent in curved microchambers. In phase 2, the cells are released from captivity and their straightening rates are measured. Before reporting our experimental results, we discuss the theoretical predictions of our model.

As discussed in detail in the Methods, using linear elasticity theory we determined the areal strain experienced by the cell wall at an angle  $\theta$  and time  $t$  in both phases 1 ('in') and 2 ('out') as:

$$A^{\text{in}}(\theta, t) \approx A_0 + A_1^{\text{in}}(B_0 - c_0) \sin \theta, \quad (1)$$

$$A^{\text{out}}(\theta, t) \approx A_0 - A_1^{\text{out}}c(t) \sin \theta$$

where  $A_0$  is a constant,  $B_0$  is the ratio of the cell radius  $r$  to the radius of curvature of a bent cell in phase 1, which is assumed small compared to unity and partially relieved by a smaller, constant differential growth parameter  $c_0 < B_0$ , and both  $A_1^{\text{in}} = 1 + \eta - \nu - \eta\nu + \eta\nu^2$  and  $A_1^{\text{out}} = \eta(2 + \eta - 2\nu - 4\eta\nu + \eta\nu^2)/4$  are positive for the parameter values relevant to *E. coli* (Supplementary Table 1). Here  $\eta = pr/Y$  is a dimensionless pressure,  $p$  is the turgor pressure,  $Y$  and  $\nu$  are, respectively, the two-dimensional elastic modulus and Poisson ratio of the cell wall, and  $\theta = \pi/2$  and  $\theta = -\pi/2$  specify, respectively, the outer and inner edges of the cell. The differential growth parameter is defined so that the arclengths of the inner and outer edges differ by  $2c_0L$ , where  $L$  is the length along the cellular midline, and the assertion that  $c_0 < B_0$  is consistent with an elastic snapback wherein removing the bending force results in a sudden decline of curvature from  $B_0/r$  to  $c_0/r$ . The variational component  $\delta A^{\text{out}} = -A_1^{\text{out}}c(t) \sin \theta$  is opposite in sign to

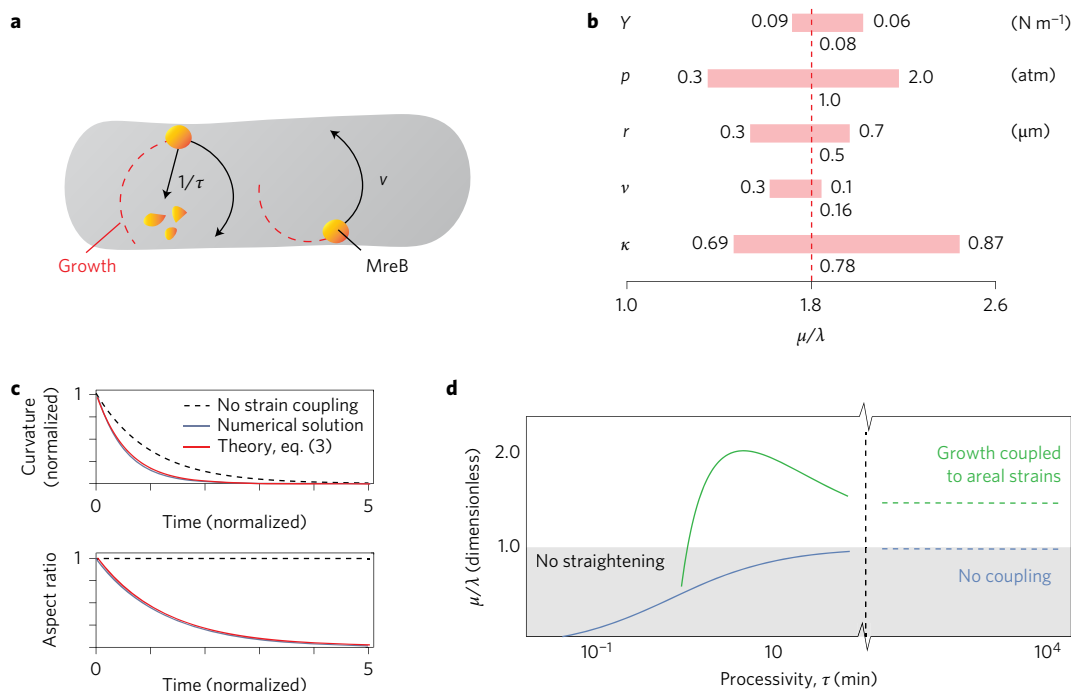


**Figure 2 | Areal strain-dependent PG elongation quantitatively predicts shape recovery dynamics.** **a**, MreB molecules are modelled as points that move circumferentially along the PG mesh with a spot velocity  $v$  and unbind as a Poisson process with rate  $1/\tau$ . The growth at angle  $\theta$  at a given time depends on the number of initiated glycan strands also at  $\theta$ , which in turn depends on the strain profile of the cell in the past (see also the growth equation in Supplementary Note 2). **b**, Sensitivity analysis of the theoretically predicted straightening rate for several material properties, assuming a large MreB processivity of  $M\tau = 6$  rad, where  $M$  is the angular velocity of an MreB filament. The elastic snapback and material parameters determine the value of the areal strain-coupling parameter  $\alpha$  self-consistently, as discussed in Supplementary Note 2. The predicted straightening rate is consistent with the experimental data shown in Fig. 3c. Here, the symbols  $\nu$  and  $\kappa$  denote the Poisson ratio and snapback ratio, respectively (to be distinguished from the MreB spot velocity,  $v$ , and the strain-independent growth rate,  $k$ ). **c**, Numerical solutions of the growth equation agree with the theoretical prediction for the straightening rate. Here, the aspect ratio is defined as the product of arclengths and curvature,  $L(t)C(t)$ , which does not decay without areal strain coupling in the limit of infinite processivity (dashed lines; also Supplementary Video 11). Normalized time is defined with units of  $1/\lambda = t_d/\ln(2)$ . **d**, There is an intermediate value of the processivity, measured in units of time for a constant rate of PG subunit insertion, for which mechanical strain sensing confers the largest effect on straightening. Empirical values of MreB processivity, intriguingly, lie close to the optimal value at which a cell straightens most quickly.

$\delta A^{in} = A_1^{in}(B_0 - c_0) \sin \theta$  and is expressed as a function of a time-dependent differential growth parameter  $c(t)$ . Importantly, the variational components in both phases 1 and 2 agree in sign with the differential growth profiles (Fig. 1c).

Given the variational areal strains, we modelled areal strain-dependent growth by assuming that the number of glycan strand initiations  $\gamma$  per unit area can be decomposed into strain-independent and strain-dependent components:

$$\gamma(\theta, t) = k + \alpha \delta A(\theta, t) \tag{2}$$

where  $k$  is a constant, strain-independent rate,  $\delta A(\theta, t)$  is the variational areal strain as a function of angle  $\theta$  and time  $t$ , and the parameter  $\alpha$  quantifies the intensity of growth-strain coupling. The average initiation rate  $k$  can be determined by factors other than strain and need not depend on mechanical stress or turgor pressure<sup>25</sup>. For instance, a growth mechanism may depend only on the abundance of PGEM constituents in maintaining an average initiation rate over the entire cell, but be biased towards regions of high strain in a manner that does not increase the average initiation rate.

To quantify the straightening rate arising from areal strain-dependent growth, we coarse-grained the growth dynamics of *E. coli* by first assuming that MreB filaments, which are spatially correlated with new glycan insertions<sup>26</sup>, correspond to PG growth sites. This is consistent with a growth scheme in which MreB filaments orchestrate persistent motion of the PGEM, but differential glycan strand initiation depends on strain-sensitive elongasome components. Although MreB filaments

have been observed to move at a helical pitch angle<sup>26</sup>, the small pitch allows us to model them as point molecules moving circumferentially along the inner membrane with a spot velocity of  $v = 5 \text{ nm s}^{-1}$ , corresponding to experimentally observed values<sup>27–29</sup> (Fig. 2a). We further modelled the decay of an MreB filament as a Poisson process with rate  $1/\tau$ , where  $\tau \approx 5 \text{ min}$  is the spatial persistence time of membrane-bound MreB (ref. 12), a value that is consistent with our snapback measurements (Supplementary Discussion). Convolution of  $\gamma$  with the width of PG inserted per growth site then yields an integro-differential growth equation describing the pole-to-pole cell length  $L(\theta, t)$  at any angle  $\theta$  and time  $t$  (see Supplementary Note 2 for a derivation and solution of this equation). As the pole-to-pole lengths determine the midline curvature  $C(t)$  at any point in time, solving the growth equation results in a theoretical prediction of the straightening rate. In the limit of large processivity, we found an approximate relation between the normalized straightening rate  $\mu = -dC/(Cd t)$ , the normalized growth rate  $\lambda = dL/(Ld t)$  and the snapback ratio  $\kappa = c_0/B_0$  as:

$$\mu \approx \lambda \left( 1 + \frac{\kappa A_1^{out}}{(1 - \kappa) A_1^{in}} \right) \tag{3}$$

Figure 2b,c illustrates the prediction of equation (3), which varies depending on processivity (Fig. 2d), for the parameter values of *E. coli* summarized in Supplementary Table 1 and a snapback ratio obtained from the experiments described below.

Previous studies examined the plastic deformation of *E. coli* cells under flow<sup>4,19</sup>, but prior experiments were limited to several cells

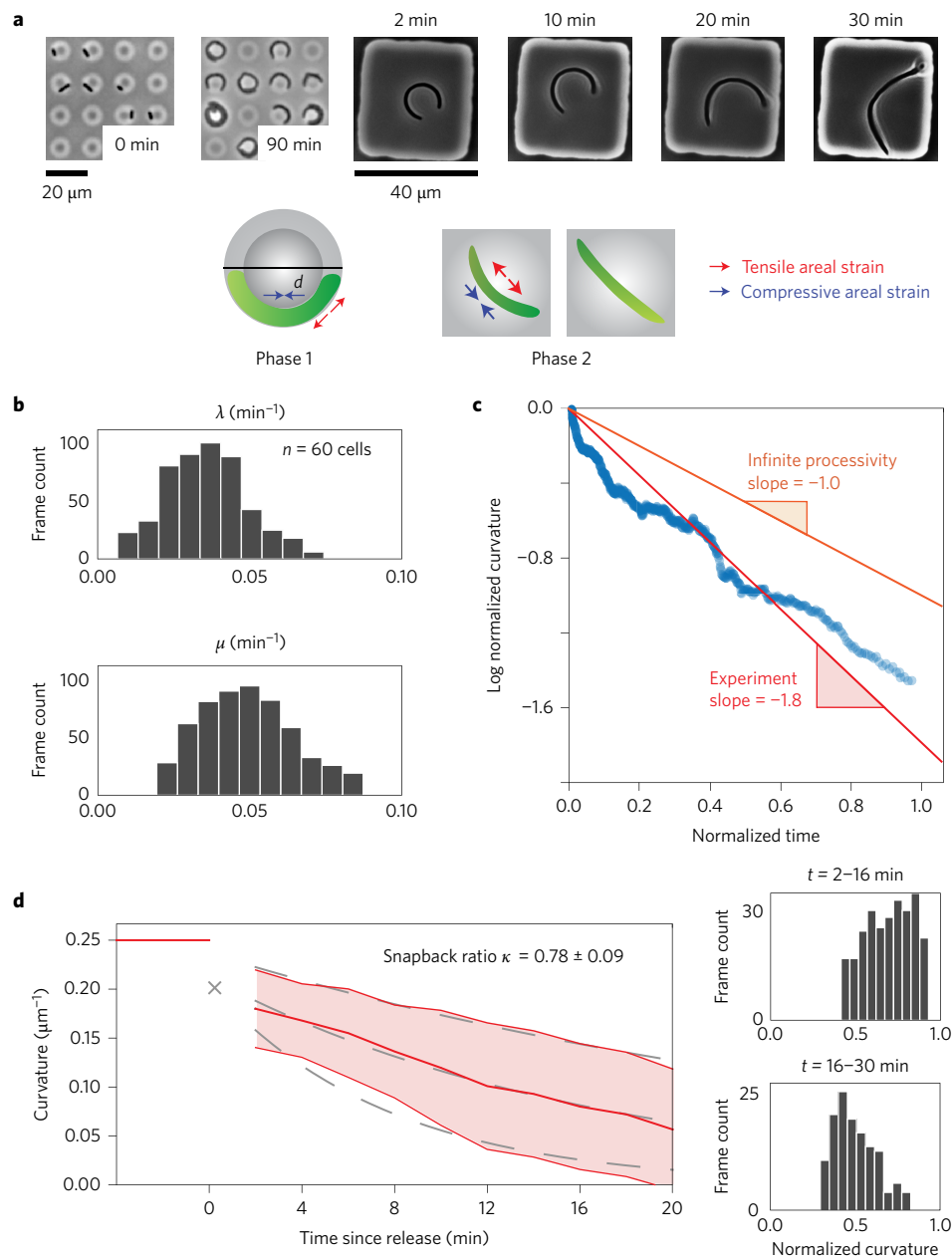


**Figure 3 | Quantitative analysis of cellular straightening dynamics.** **a**, In our experiments, filamentous *E. coli* cells were grown in confined, toroidal microchambers of diameter  $d = 8 \mu\text{m}$ . An elastic snapback was observed upon removal, after which the cells recovered their straight, rod-like morphologies over time. Images correspond to before (0 and 90 min) and after (2, 10, 20 and 30 min) microchamber release. **b**, Histograms for the instantaneous growth rate  $\lambda = dL/(Ldt)$  and instantaneous straightening rate  $\mu = -dC/(Cdt)$  for 60 *E. coli* cells. **c**, Plot of log normalized curvature, defined as  $\ln(C(t)/C(2 \text{ min}))$ , as a function of time since release (in units of  $t_d/\ln(2)$ ) for all 60 cells in phase 2. A 50-point moving average filter along the temporal direction was applied to smooth out the data. The population-averaged straightening-to-growth ratio is  $\langle \mu \rangle / \langle \lambda \rangle = 1.8$ , which cannot be explained by an infinite processivity of PG synthesis. The slower rate of decrease of the log normalized curvature for large times may be an artefact of substrate pinning for large cells. **d**, Left: extrapolating the population-averaged curvature to the time of microchamber release at  $t = 0$  yields a mean elastic snapback ratio of  $\kappa = 0.78 \pm 0.09$  (as denoted by the 'x'). Shaded areas denote values within one standard deviation of the population mean. Grey dashed lines denote exponential fits to values that are one standard deviation away from the population average. Right: distributions of aggregated normalized curvatures  $C(t)/C(0)$  at times  $t = 2\text{--}16$  min and  $t = 16\text{--}30$  min.

and the areal strains were non-uniform in the axial directions of the cells. To test our theory of strain-dependent growth, we therefore conducted experiments following the two phases described above. In phase 1, filamentous *E. coli* cells grew in toroidal microchambers with constant diameters of  $d = 8 \mu\text{m}$  (Fig. 3a). The cells were confined to the microchambers during growth and extracted into a larger, square-shaped microchamber once they filled over 90% of the microchamber circumference. Elastic snapbacks of the cells

were observed after extraction, in agreement with flow-based experiments<sup>4</sup> (Supplementary Discussion). In phase 2, we imaged the shape recovery process of unconfined cells in 2 min intervals for over 40 min (Supplementary Videos 1–10).

On imaging the recovery process, we quantitatively analysed the straightening dynamics of unconfined phase 2 cells (the methodology and results are detailed in the Supplementary Methods and Supplementary Fig. 7). We extracted the normalized growth rate  $\lambda$

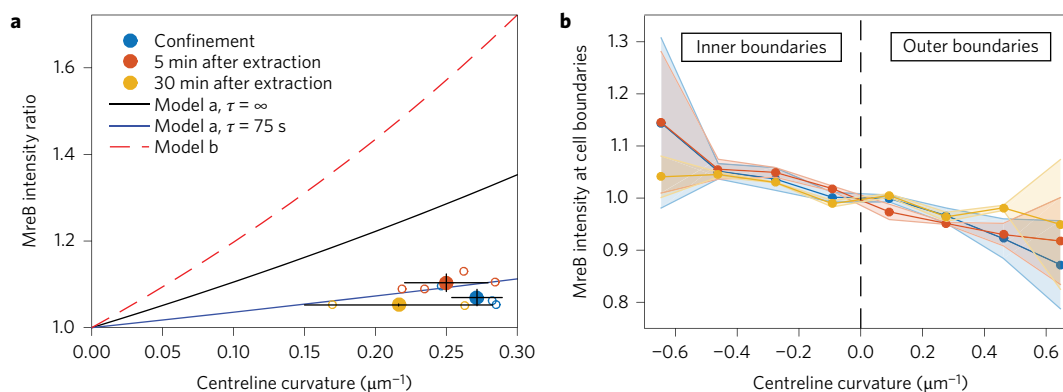


**Figure 4 | MreB-*msfGFP* fusion cells exhibit MreB enrichment at negative Gaussian curvature, but MreB enrichment alone cannot explain straightening.**

**a**, MreB is predominantly localized at the inner edges of filamentous MreB-*msfGFP* *E. coli* cells. Shown is the MreB-*msfGFP* intensity ratio between the inner and outer cell edges, measured in confinement, after release from confinement and 30 min into recovery. For each condition, open circles indicate averages obtained from at least 15 cells per replicate experiment, as detailed in the Methods. Filled circles indicate averages over replicates and error bars indicate standard deviations between replicates. Solid curves indicate the predicted MreB intensity ratio for a model of constant MreB initiation rate and different processivity times  $\tau$ , assuming a spot velocity of  $v = 5 \text{ nm s}^{-1}$  (model a in the legend; for details see Supplementary Note 2). The dashed line indicates the MreB intensity ratio that would be required to account for the observed straightening ratio of 1.8 within a model where cell wall synthesis depends only on MreB localization (model b in the legend). Thus, MreB localization is consistent with a model of constant initiation and finite processivity and the observed intensity ratio is not sufficient to account for cell straightening. **b**, MreB-*msfGFP* intensities decrease as a function of signed centreline curvature where the inner and outer edges of a cell correspond to negative and positive values of centreline curvature, respectively. Error bars denote standard deviations, as in **a**.

from the arclengths of the resulting fits for 60 cells and found a population-averaged value of  $\langle \lambda \rangle = 0.021 \text{ min}^{-1}$  (Fig. 3b,c and Supplementary Fig. 8). This value of  $\langle \lambda \rangle$  reflects a doubling time of  $t_d = 33 \text{ min}$ , in agreement with bulk culture growth measurements<sup>30,31</sup>. Similarly, we extracted the normalized straightening rate  $\mu$  from the curvatures of the fits and found a population-averaged value of  $\langle \mu \rangle = 0.038 \text{ min}^{-1}$ , 1.8 times larger than the growth rate. Extrapolating the population-averaged curvature to the time of release, two minutes before the first frame, yields a mean elastic snapback ratio of  $\kappa = 78\%$ , with an extrapolated standard deviation of 9% (Fig. 3d). The observed straightening rate and snapback ratio are consistent with equation (3) (Fig. 2b,c) and numerical simulations of the growth process (Supplementary Figs 5 and 6 and Supplementary Video 11) for the material values of *E. coli* summarized in Supplementary Table 1.

We next wondered whether MreB—which is believed to localize to regions of negative Gaussian curvature in cells with submicrometre-scale indentations<sup>12</sup>—could also sense strain or otherwise account for straightening by localizing to the inner edge in unconfined phase 2 cells. To test the possibility that MreB localization could explain cell straightening, we repeated the foregoing experiments with a fully functional and complementing MreB-*msfGFP* fusion expressed from the native *mreB* locus<sup>32</sup>. We measured MreB fluorescence intensities at the inner and outer edges of both phase 1 and 2 cells using an approach similar to previous work<sup>12</sup> (see Supplementary Methods and Supplementary Figs 9 and 10 for details). In qualitative agreement with previous work<sup>12</sup>, we found increased MreB-*msfGFP* intensities at the inner edges of confined phase 1 cells (Fig. 4a), with an enrichment positively correlated with the centreline curvature (Fig. 4b), indicating that MreB localization alone cannot account for growth inside confinement in phase 1. We also found an increased MreB-*msfGFP* intensity at the inner edges of recovering phase 2 cells. However, the MreB enrichment is not sufficient to explain a straightening ratio of 1.8 based on a model in which cell elongation is proportional to MreB density (Fig. 4a). Together, these results indicate that MreB localization cannot explain differential growth in both phases 1 and 2. Furthermore, although we do not rule out an active mechanism for curvature-sensing in submicrometre-scale indentations, the observed MreB localization between the inner and outer edges of

bent cells does not require an active sensing mechanism but can be explained by constant initiation and persistent circumferential motion alone (Fig. 4a).

The consistency of our strain-based model with experimental results suggests that mechanical strains arising from differential growth can act as a sensory cue for robust shape regulation. Subsequent simulations and stress analyses indicate that other sources of variation in elastic quantities, particularly non-uniform crosslinking of glycan strands or cleavage of peptide bonds, cannot explain the observed straightening rate (Supplementary Note 1 and Supplementary Figs 3 and 4). However, while our results constrain models that can explain straightening, further work will be needed to experimentally demonstrate that mechanical strain mediates PG elongation and uncover the molecular mechanisms responsible for mechanical strain sensing. One intriguing possibility for such a mechanism is the lipoprotein-PBP interaction, which may be sensitive to PG pore size<sup>9,33–35</sup>. We anticipate future experiments to determine possible effects of the lipoprotein-PBP interaction and other perturbations, such as osmotic shock (Supplementary Discussion and Supplementary Fig. 11), on straightening.

In summary, we have used a combination of theory and experiment to quantitatively reveal and explain shape recovery in cells that have been released after growing in a confined environment. Our findings underscore how perturbing cells using physical, in contrast to biological, approaches can uncover how cells function in their native conformations. Because cell wall strains are determined by the entire deformation history of the cell, strain-sensitive growth can enable the robust recovery of native rod shape<sup>3,4,13,14</sup>, in addition to allowing cells to adapt to growth in various geometries by relieving cell wall stresses and regulating cell wall thickness by localizing growth to thinner regions of PG, where the areal strains are larger. By showing that coupling growth to mechanical strain can quantitatively explain shape recovery, our analysis contributes to our understanding of the possible biophysical mechanisms that underlie the remarkable diversity and robustness of cellular morphology.

## Methods

**Areal strain profiles of a cell in phases 1 and 2.** To quantify the areal strain incurred by a bent, filamentous cell due to non-uniform growth, we modelled the bacterial cell

wall as a homogeneous, isotropic, linear-elastic shell under pressure. For the spatial coupling of growth to regions of high areal strain to be consistent with the elastic snapback observed in previous flow-based experiments (Fig. 1b), it is necessary that a bending force makes the areal strain larger on the outer edge of the cell. It is also necessary that the residual stresses caused by turgor pressure and anisotropic growth during bending make the areal strain smaller on the outer edge once the bending force is removed. A mechanical-strain-dependent growth rate, in which the initiation rate of new glycan strands quantitatively depends on the areal strain, would then explain the ability of the cell to both plastically adapt to a bending force and straighten in the absence of external forces.

When a cell is bent uniformly by an external force (phase 1), the areal strain, which is sinusoidally varying in the azimuthal coordinate  $\theta$  and constant in the axial direction, is readily determined by elasticity theory and is larger on the outer edge due to the axial stresses incurred by bending (Supplementary Note 1 and Supplementary Fig. 1). Determining the areal strain once the bending force is removed (phase 2) requires consideration of growth as the cell is bent. It is convenient to model growth by changing the intrinsic geometry of the cell, which is the shape a cell would assume in the absence of external forces such as pressure<sup>36,37</sup>. Any growth in the axial direction that couples to a sinusoidally varying areal strain profile is also sinusoidally varying, so the intrinsic pole-to-pole PG length becomes larger at the outer edge and smaller at the inner edge in phase 1 (Fig. 1c). As a result of this differential growth, the intrinsic geometry of the cell evolves from that of a cylinder to that of a torus, a geometry for which the pole-to-pole lengths are sinusoidally varying. The toroidal geometry is described by the cell radius  $r$  and a differential growth parameter  $c$ , which quantifies the cellular growth asymmetry.

Assuming that growth does not change the elastic properties of a cell, the areal strain of a phase 2 cell can be determined. Although the shape of a circular torus would exactly realize the intrinsic geometry resulting from differential growth, the presence of a turgor pressure can result in a different geometry and stress state. We therefore undertook finite-element stress analyses of a closed, circular toroidal shell section subject to internal pressure (see Supplementary Methods for a detailed discussion of the simulation methodology and results). We found that, for both infinitesimal and moderate strains, the stress profiles were well approximated by the linear theory result in which the deformed geometry remains that of a circular torus (Fig. 1c and Supplementary Fig. 2), with a circumferential stress component that is larger on the inner edge. Interestingly, the sources of the variational terms  $\delta A^{\text{in}}$  and  $\delta A^{\text{out}}$  are the axial and circumferential components of the stress tensor, respectively, and neither one of the variational stress components alone flips signs between phases 1 and 2 (Supplementary Note 1).

**Equilibrium simulations of an elastic shell.** Stress analyses of closed cylindrical and toroidal shells subject to internal pressure were computationally undertaken with finite-element simulations using Abaqus FEA (Dassault Systems). Explicit details of these simulations are discussed in the Supplementary Methods. Abaqus input files were created with MATLAB, with shells being discretized uniformly into approximately 10,000 S4R elements, assigned material properties faithful to that of the *E. coli* cell wall, and equilibrated with respect to a range of internal pressures and material parameters. The axial and circumferential stress resultants were then extracted from the deformed state and used to compute the areal strain.

**Numerical solutions of the growth equation.** Numerical solutions of the growth equation were found in MATLAB by discretizing the integral as a Riemann sum and subjecting two time series, one for each of the lengths of the inner and outer edges of the cell, to the specified difference equation. The curvature along the midline is obtained as  $C(t) = (L(\pi/2, t) - L(-\pi/2, t)) / (r(L(\pi/2, t) + L(-\pi/2, t)))$ , where  $L(\theta, t)$  is the pole-to-pole length at angle  $\theta$  and time  $t$ , and  $r$  is the cell radius. Discrete simulations of the growth process were also undertaken, as discussed in the Supplementary Methods, and are summarized in Supplementary Fig. 5 and Supplementary Video 11.

**Microfabrication.** We designed patterns of microchambers in doughnut-shaped designs in CleWin (Delta Mask) and square-shaped designs in Adobe Illustrator (Adobe Systems). The design of the doughnut-shaped microchambers was inspired by previous work<sup>20</sup>. We created designs of doughnuts with outer diameters of 8  $\mu\text{m}$  (channel width 2  $\mu\text{m}$ ), corresponding to circumferences of  $\sim 25 \mu\text{m}$  (Fig. 2a). The number of doughnut-shaped microchambers was  $\sim 40,000$  per array. The microfabrication process has been reviewed in detail in ref. 38 and previously described for microchannels and microchambers<sup>18,39</sup>. Pristine silicon dioxide wafers were cleaned in isopropanol and ddH<sub>2</sub>O repeatedly. For doughnut-shaped microchambers, we used positive photoresist Shipley 1813 (MicroChem). Before spincoating, a vapour of hexamethyldisilazane (HMDS) was deposited on the clean silicon dioxide wafer substrate to prime it for adhesion of the photoresist. The spincoating resulted in  $\sim 1.3\text{-}\mu\text{m}$ -thick layers of photoresist. For square-shaped microchambers, we used negative photoresist SU8-3010 (MicroChem) directly spincoated onto clean silicon dioxide wafers to produce  $\sim 20\text{-}\mu\text{m}$ -thick polymer layers. Layer thicknesses were confirmed using a surface profilometer (Tencor AlphaStep 200). Doughnut-shaped microchambers were directly written onto the photoresists by laser lithography ( $\mu\text{PG}$  101, Heidelberg Instruments). Photomasks (CAD/Art Services) were used for the transfer of square-shaped microchambers onto the photoresist using UV lithography. The patterns were developed with

MF-321 and SU-8 developer (MicroChem), respectively. The resulting photoresist master was silanized overnight using a vapour of (tridecafluoro-1,1,2,2-tetrahydroxyethyl)trichlorosilane (Gelest). Applying soft lithography<sup>40</sup>, we transferred the pattern into polydimethylsiloxane (PDMS) (Sylgard 184, Dow Corning) using a ratio of 10:1 (base to curing agent) and cured the polymer overnight at 60 °C. The resulting PDMS layer contained patterns of microchambers in bas-relief and was used as a stamp to emboss a layer of agarose or agar<sup>20</sup> for bacteria cell growth. We poured a hot solution (65 °C) of 4% lysogeny broth (LB)-agarose (EM-2120, Omnipur, EM Biosciences) containing isopropyl- $\beta$ -D-1-thiogalactopyranoside (IPTG, Sigma Aldrich) and antibiotics (if required) on PDMS stamps oriented with the features facing up and cooled them to room temperature to gel the agarose. We cut out the layer of LB-agarose embossed with microchambers using a scalpel and prepared the microchambers for growth experiments.

**Bacterial strains and growth.** *E. coli* MG1655 was used with plasmid encoding SulA (a cell division inhibitor<sup>41,42</sup>) under an inducible lac promoter to induce filamentation with 1 mM IPTG. Bacteria were grown in liquid LB<sup>43,44</sup> (10 g l<sup>-1</sup> tryptone, 5 g l<sup>-1</sup> yeast extract, 10 g l<sup>-1</sup> NaCl) and, if required, supplemented with appropriate antibiotics. LB medium containing 1.5% Difco agar (wt/vol) was used to grow individual colonies. Tryptone, yeast extract, peptone, Petri dishes and bacteriological agar were purchased from Becton Dickinson and sodium chloride from Fisher Scientific. Bacteria were grown from a single colony in LB at 30 °C overnight and the medium was supplemented with 100  $\mu\text{g ml}^{-1}$  ampicillin (Sigma Aldrich) for plasmid selection. We used a 1:1,000 dilution to inoculate fresh liquid LB medium. The culture was grown at 30 °C with shaking at 200 r.p.m. to an absorbance of  $\sim 0.6$  ( $\lambda = 600 \text{ nm}$ ). At this point, we added IPTG to a final concentration of 1 mM and incubated the solution for another 5 min to initiate filamentation (expression of SulA) under shaking at 30 °C. Subsequently, we added  $\sim 3\text{-}5 \mu\text{l}$  of the bacterial culture to the top of the doughnut-shaped microchambers (embossed in LB agarose with 1 mM IPTG, no antibiotics), incubated the agarose slab for 30 s, and sealed the microchambers with a #1.5 cover slip (12-548-5g, Fisher Scientific). The microchambers were incubated in a static incubator at 30 °C for at least 2 h and the progress of filamentation was monitored every 20 min thereafter. Once the majority of cells were sufficiently filamented, we cut out the doughnut-shaped microchambers from the LB-agarose slab with a scalpel. We placed a 10  $\mu\text{l}$  drop of LB-IPTG solution on a clean glass coverslip, used tweezers to hold the LB-agarose slab, and lifted the microchambers in and out of the drop to release the cells from the microchambers. We repeated this step at least 20 times. The remaining drop was pipetted carefully, added on top of the square-shaped microchambers and sealed with a coverslip. We then immediately started imaging of the recovery process. Note that we also used *E. coli* MG1655 with the addition of 20  $\mu\text{g ml}^{-1}$  cephalixin as we have done successfully before for spheroplast formation<sup>39</sup>. However, genetic manipulation generated fewer perturbations during the filamentation process and we observed frequent cell lysis under antibiotic pressure even at low cephalixin concentrations.

The MreB-msfGFP strain used for MreB localization experiments carries a functional MreB-msfGFP translational sandwich fusion in the native mreB locus (MG1655, mreB'-msfGFP<sup>SW</sup>-mreB'), as previously described and characterized<sup>32</sup>, and the same pSulA plasmid described above to inhibit cell division. For MreB localization experiments, the MreB-msfGFP strain was grown overnight from frozen stock at 37 °C in LB plus ampicillin (100  $\mu\text{g ml}^{-1}$ ) in a shaking incubator. The overnight culture was washed and diluted 1:500 in M63 minimal medium<sup>45</sup> containing glucose (0.4% wt/vol), NH<sub>4</sub> (20 mM), casamino acids (0.2%wt/vol) and ampicillin (100  $\mu\text{g ml}^{-1}$ ). M63 medium was used during MreB localization experiments for enhanced fluorescence, and liquid LB, as described above, was used otherwise. The difference in medium is not expected to affect our results, as elastic snapback measurements and MreB motion are robust over a range of growth conditions<sup>4,27</sup>. The culture was grown at either 37 °C or 30 °C, as indicated, to an optical density at 600 nm (OD<sub>600</sub>) of 0.1 in the shaker. Then, 1 mM IPTG was added to induce SulA expression and cells were grown for approximately half a doubling time ( $\sim 20 \text{ min}$  at 37 °C or  $\sim 40 \text{ min}$  at 30 °C) in the shaker before being collected for microchamber confinement and microscopy. MreB-msfGFP intensity measurements were performed on cells grown in minimal medium for reduced autofluorescence and at 37 °C for increased growth rates. We confirmed that cells grown at 30 °C behave quantitatively similarly in terms of their average curvature and MreB enrichment, during confinement and after release from the microchambers (Supplementary Table 2).

**Microscopy.** We used a Zeiss Axiovert 200 inverted microscope with an enclosing custom-made incubation chamber (at 30 and 37 °C) equipped with an AxioCam 503 mono charge-coupled device (CCD, Zeiss) and a 40 $\times$  objective (EC Plan-neofluar, NA 0.75). Imaging was confined to square microchambers of length 40  $\mu\text{m}$ . The time between each frame during timelapse measurements was 2 min. Images were recorded using AxioVision (v.4.8, Zeiss). ImageJ (NIH) was used for cropping raw timelapse images and to export the files as image sequences.

MreB-msfGFP cells were confined in toroidal microchambers of 8  $\mu\text{m}$  outer diameter and 2  $\mu\text{m}$  inner diameter, similar to the experiments described above (but with a smaller inner diameter). In contrast, the agarose microchambers used were made from M63 minimal medium containing IPTG. To study MreB localization in

confinement, cells were grown in microchambers for approximately two doubling times (~80 min at 37 °C or ~160 min at 30 °C) before imaging. At this time, cells had an average length of ~10 µm (Supplementary Table 2). Subsequently, cells were extracted in the same way as described above. Extracted cells were sandwiched between a flat 1% M63 agarose pad and a cover glass for cell immobilization and microscopy. During the time from cell extraction to imaging (~5 min), cells were maintained at room temperature to minimize elongation. To study MreB localization during recovery, extracted cells were incubated in M63 minimal medium for the indicated time in PCR tubes at 37 °C before being placed and imaged on M63 agarose pads in the same manner as immediately after extraction. MreB–msfGFP cells were imaged by phase-contrast and epifluorescence microscopy using an inverted microscope (TI-E, Nikon) equipped with a 100× phase contrast objective (CFI Plan Apo Lambda DM 100× 1.4 NA, Nikon), a solid-state light source (Spectra X, Lumencor), a multiband dichroic (69002bs, Chroma Technology) and excitation (485/25) and emission (535/50) filters. Images were acquired using a sCMOS camera (Orca Flash 4.0, Hamamatsu) with an effective pixel size of 65 nm.

Imaging data were acquired for 132 non-fusion cells over 24 replicate experiments, of which 60 were analysed (Fig. 3), and ~70 cells under osmotic shock over six replicate experiments, of which 49 were analysed (Supplementary Fig. 11). As discussed below, the cells that were analysed were selected because their curvatures were quantified accurately by our image analysis. We performed four experiments with 34, 18, 48 and 19 MreB–msfGFP cells, four experiments with 33, 34, 30 and 35 MreB–msfGFP cells, and two experiments with 17 and 15 MreB–msfGFP cells for the confinement, 5 min after extraction and 30 min after extraction cases, respectively, in Fig. 4.

**Shape analysis.** Cell identification, outlining and skeleton detection for the length and curvature measurements were performed using a custom-made, MATLAB-based software package called CurvatureTracker, which is available upon request. We found that pre-existing software, such as MicrobeTracker<sup>46</sup>, did not provide adequate tools for automating the collection of curvature data required in this work. CurvatureTracker uses Sobel edge detection, morphological opening, cluster analysis and thresholding for an initial guess, followed by a custom optical flow algorithm for detecting the cell in subsequent frames. An orientation for the skeleton, required for a parametric fit, was induced using a nearest-neighbour algorithm and connecting disparate connected components according to local orientation and distance. A sweepline algorithm was used to determine the overall orientation. To measure the straightening rate, we analysed a total of 60 cells, which CurvatureTracker was able to track perfectly. CurvatureTracker often failed to track image sequences with multiple cells, excessive noise, poor resolution or cells growing out of plane. By parametrically fitting the set of points  $T$  lying on the midline to a ninth-degree polynomial  $(x(t), y(t))$  using MATLAB's native fit function, we calculated the cell length using MATLAB's native hypot function and the curvature according to  $C = \sum_{t \in T} |(x'(t))y''(t) - y'(t)x''(t)| / ((x'(t)^2 + y'(t)^2)^{3/2})|_{t=t'}$ . Because the ninth-degree polynomial fit may capture excessive curvature fluctuations within the mid-section of a cell, we repeated our analysis with a global arc fit to the midline. We found similar results for the global fit, which suggests a lack of substantial cell-substrate pinning or single-cell curvature fluctuations (Supplementary Fig. 8). Details of the analysis of the MreB fluorescence experiments are provided in the Supplementary Methods.

**Data availability.** The data that support the findings of this study are available from the corresponding authors upon request.

Received 2 August 2016; accepted 16 June 2017;  
published 24 July 2017

## References

- Cabeen, M. T. & Jacobs-Wagner, C. Bacterial cell shape. *Nat. Rev. Microbiol.* **3**, 601–610 (2005).
- Young, K. D. The selective value of bacterial shape. *Microbiol. Mol. Biol. Rev.* **70**, 660–703 (2006).
- Amir, A. & van Teeffelen, S. Getting into shape: how do rod-like bacteria control their geometry? *Syst. Synth. Biol.* **8**, 227–235 (2014).
- Amir, A., Bahaipour, F., McIntosh, D. B., Nelson, D. R. & Jun, S. Bending forces plastically deform growing bacterial cell walls. *Proc. Natl Acad. Sci. USA* **111**, 5778–5783 (2014).
- Garner, E. C. *et al.* Coupled, circumferential motions of the cell wall synthesis machinery and MreB filaments in *B. subtilis*. *Science* **333**, 222–225 (2011).
- Dominguez-Escobar, J. *et al.* Processive movement of MreB-associated cell wall biosynthetic complexes in bacteria. *Science* **333**, 225–228 (2011).
- Lee, T. K. *et al.* A dynamically assembled cell wall synthesis machinery buffers cell growth. *Proc. Natl Acad. Sci. USA* **111**, 4554–4559 (2014).
- Paradis-Bleau, C. *et al.* Lipoprotein cofactors located in the outer membrane activate bacterial cell wall polymerases. *Cell* **143**, 1110–1120 (2010).
- Typos, A. *et al.* Regulation of peptidoglycan synthesis by outer-membrane proteins. *Cell* **143**, 1097–1109 (2010).

- Reshes, G., Vanounou, S., Fishov, I. & Feingold, M. Cell shape dynamics in *Escherichia coli*. *Biophys. J.* **94**, 251–264 (2008).
- Bartlett, T. M. *et al.* A periplasmic polymer curves *Vibrio cholerae* and promotes pathogenesis. *Cell* **168**, 172–185 (2017).
- Ursell, T. S. *et al.* Rod-like bacterial shape is maintained by feedback between cell curvature and cytoskeletal localization. *Proc. Natl Acad. Sci. USA* **111**, 1025–1034 (2014).
- Amir, A. & Nelson, D. R. Dislocation-mediated growth of bacterial cell walls. *Proc. Natl Acad. Sci. USA* **109**, 9833–9838 (2012).
- Si, F., Li, B. & Sun, S. X. Bacterial growth and shape regulation by external compression. *Sci. Rep.* **5**, 11367 (2015).
- Meeske, A. J. *et al.* SEDS proteins are a widespread family of bacterial cell wall polymerases. *Nature* **537**, 634–638 (2016).
- Cho, H. *et al.* Bacterial cell wall biogenesis is mediated by SEDS and PBP polymerase families functioning semi-autonomously. *Nat. Microbiol.* **1**, 16172 (2016).
- Nguyen, L. T., Gumbart, J. C., Beeby, M. & Jensen, G. J. Coarse-grained simulations of bacterial cell wall growth reveal that local coordination alone can be sufficient to maintain rod shape. *Proc. Natl Acad. Sci. USA* **112**, E3689–E3698 (2015).
- Renner, L. D., Eswaramoorthy, P., Ramamurthi, K. S. & Weibel, D. B. Studying biomolecule localization by engineering bacterial cell wall curvature. *PLoS ONE* **8**, e84143 (2013).
- Caspi, Y. Deformation of filamentous *Escherichia coli* cells in a microfluidic device: a new technique to study cell mechanics. *PLoS ONE* **9**, e83775 (2014).
- Takeuchi, S., DiLuzio, W. R., Weibel, D. B. & Whitesides, G. M. Controlling the shape of filamentous cells of *Escherichia coli*. *Nano Lett.* **5**, 1819–1823 (2005).
- Mannik, J., Driessen, R., Galajda, P., Keymer, J. E. & Dekker, C. Bacterial growth and motility in sub-micron constrictions. *Proc. Natl Acad. Sci. USA* **106**, 14861–14866 (2009).
- Cabeen, M. T. *et al.* Bacterial cell curvature through mechanical control of growth. *EMBO J.* **28**, 1208–1219 (2009).
- Sliusarenko, O., Cabeen, M. T., Wolgemuth, C. W., Jacobs-Wagner, C. & Emonet, T. Processivity of peptidoglycan synthesis provides a built-in mechanism for the robustness of straight-rod cell morphology. *Proc. Natl Acad. Sci. USA* **107**, 10086–10091 (2010).
- Mukhopadhyay, R. & Wingreen, N. S. Curvature and shape determination of growing bacteria. *Phys. Rev. E* **80**, 062901 (2009).
- Rojas, E., Theriot, J. A. & Huang, K. C. Response of *Escherichia coli* growth rate to osmotic shock. *Proc. Natl Acad. Sci. USA* **111**, 7807–7812 (2014).
- Wang, S., Furchtgott, L., Huang, K. C. & Shaevitz, J. W. Helical insertion of peptidoglycan produces chiral ordering of the bacterial cell wall. *Proc. Natl Acad. Sci. USA* **109**, 595–604 (2012).
- van Teeffelen, S. *et al.* The bacterial actin MreB rotates, and rotation depends on cell-wall assembly. *Proc. Natl Acad. Sci. USA* **108**, 15822–15827 (2011).
- Harris, L. K., Dye, N. A. & Theriot, J. A. A *Caulobacter* MreB mutant with irregular cell shape exhibits compensatory widening to maintain a preferred surface area to volume ratio. *Mol. Microbiol.* **94**, 988–1005 (2014).
- Kim, S. Y., Gitai, Z., Kinkhabwala, A., Shapiro, L. & Moerner, W. E. Single molecules of the bacterial actin MreN undergo directed treadmilling motion in *Caulobacter crescentus*. *Proc. Natl Acad. Sci. USA* **103**, 10929–10934 (2006).
- Tuson, H. H. *et al.* Measuring the stiffness of bacterial cells from growth rates in hydrogels of tunable elasticity. *Mol. Microbiol.* **85**, 874–891 (2012).
- Stewart, E. J., Madden, R., Paul, G. & Taddei, F. Aging and death in an organism that reproduces by morphologically symmetric division. *PLoS Biol.* **3**, e45 (2005).
- Ouzounov, N. *et al.* MreB orientation correlates with cell diameter in *Escherichia coli*. *Biophys. J.* **111**, 1035–1043 (2016).
- Paradis-Bleau, C. *et al.* Lipoprotein cofactors located in the outer membrane activate bacterial cell wall polymerases. *Cell* **143**, 1110–1120 (2010).
- Egan, A. J. F. *et al.* Outer-membrane lipoprotein LpoB spans the periplasm to stimulate the peptidoglycan synthase PBP1B. *Proc. Natl Acad. Sci. USA* **111**, 8197–8202 (2014).
- Lee, T. K., Meng, K., Shi, H. & Huang, K. C. Single-molecule imaging reveals modulation of cell wall synthesis dynamics in live bacterial cells. *Nat. Commun.* **7**, 13170 (2016).
- Efrati, E., Sharon, E. & Kupferman, R. The metric description of elasticity in residually stressed soft materials. *Soft Matter* **9**, 8187–8197 (2013).
- Santangelo, C. D. Buckling thin disks and ribbons with non-Euclidean metrics. *EPL* **86**, 34003 (2009).
- Weibel, D. B., Diluzio, W. R. & Whitesides, G. M. Microfabrication meets microbiology. *Nat. Rev. Microbiol.* **5**, 209–218 (2007).
- Renner, L. D. & Weibel, D. B. Cardiolipin microdomains localize to negatively curved regions of *Escherichia coli* membranes. *Proc. Natl Acad. Sci. USA* **108**, 6264–6269 (2011).
- Xia, Y. & Whitesides, G. M. Soft lithography. *Angew. Chem. Int. Ed.* **37**, 550–575 (1998).
- Huang, J., Cao, C. & Lutkenhaus, J. Interaction between FtsZ and inhibitors of cell division. *J. Bacteriol.* **178**, 5080–5085 (1996).

42. Huisman, O., D'Ari, R. & Gottesman, S. Cell-division control in *Escherichia coli*: specific induction of the SOS function SfiA protein is sufficient to block septation. *Proc. Natl Acad. Sci. USA* **81**, 4490–4494 (1984).
43. Bertani, G. Studies on lysogenesis. I. The mode of phage liberation by lysogenic *Escherichia coli*. *J. Bacteriol.* **62**, 293–300 (1951).
44. Bertani, G. Lysogeny at mid-twentieth century: P1, P2, and other experimental systems. *J. Bacteriol.* **186**, 595–600 (2004).
45. Miller, J. H. *Experiments in Molecular Genetics* (Cold Spring Harbor, 1972).
46. Sliusarenko, O., Heinritz, J., Emonet, T. & Jacobs-Wagner, C. High-throughput, subpixel precision analysis of bacterial morphogenesis and intracellular spatio-temporal dynamics. *Mol. Microbiol.* **80**, 612–627 (2011).

### Acknowledgements

F.W. was supported by the National Science Foundation Graduate Research Fellowship under grant no. DGE1144152. L.D.R., S.v.T. and A.A. were supported by the Volkswagen Foundation. G.O. and S.v.T. were supported by funds from the European Research Council (ERC-2015-STG RCSB 679980), the LabEx IBEID (Integrative Biology of Emerging Infectious Diseases) programme, the Mairie de Paris 'Emergence(s)' programme, and the ANR 'Investissement d'Avenir Programme' (10-LABX-62-IBEID) to S.v.T. J.P. acknowledges funding by a Delta ITP Zwaartekracht grant. A.A. was supported by the Alfred P. Sloan Foundation. The authors thank J. Hutchinson for discussions on shell theory, J. Hutchinson, E.C. Garner and C. Wivagg for comments on the manuscript, L. Mahadevan and C. Wivagg for discussions on the model, K. Bertoldi and J. Liu for help

with simulation software, E. Oldewurtel and E. Brambilla for help with microscopy and N. Ouzounov for providing the MreB-msfGFP strain.

### Author contributions

F.W. and A.A. developed the model of straightening. F.W. and J.P. performed simulations. L.D.R., G.Ö., D.B.W., S.v.T. and A.A. designed the experiments. L.D.R. and G.Ö. performed the experiments. F.W., L.D.R. and G.Ö. analysed the data. F.W. and G.Ö. wrote cell-tracking software. F.W., L.D.R., G.Ö., S.v.T. and A.A. wrote the paper.

### Additional information

Supplementary information is available for this paper.

Reprints and permissions information is available at [www.nature.com/reprints](http://www.nature.com/reprints).

Correspondence and requests for materials should be addressed to L.D.R. and A.A.

**How to cite this article:** Wong, F. *et al.* Mechanical strain sensing implicated in cell shape recovery in *Escherichia coli*. *Nat. Microbiol.* **2**, 17115 (2017).

**Publisher's note:** Springer Nature remains neutral with regard to jurisdictional claims in published maps and institutional affiliations.

### Competing interests

The authors declare no competing financial interests.

In the format provided by the authors and unedited.

# Mechanical strain sensing implicated in cell shape recovery in *Escherichia coli*

Felix Wong<sup>1,†</sup>, Lars D. Renner<sup>2,3,†,\*</sup>, Gizem Özbaykal<sup>4</sup>, Jayson Paulose<sup>5</sup>, Douglas B. Weibel<sup>3,6</sup>, Sven van Teeffelen<sup>4</sup>, and Ariel Amir<sup>1,\*</sup>

<sup>1</sup>School of Engineering and Applied Sciences, Harvard University, Cambridge, MA 02138, USA

<sup>2</sup>Leibniz Institute of Polymer Research and the Max Bergmann Center of Biomaterials, 01069 Dresden, Germany

<sup>3</sup>Department of Biochemistry, University of Wisconsin-Madison, Madison, WI 53706, USA

<sup>4</sup>Department of Microbiology, Institut Pasteur, 75724 Paris, France

<sup>5</sup>Instituut-Lorentz for Theoretical Physics, Leiden University, Leiden, The Netherlands

<sup>6</sup>Department of Biomedical Engineering, University of Wisconsin-Madison, Madison, WI 53706, USA

†These authors contributed equally to this work.

\*Corresponding authors: Lars D. Renner (renner@ipfdd.de), Ariel Amir (arielamir@seas.harvard.edu)

## Supplementary Note 1

We desire to quantify the residual stresses due to anisotropic, differential growth in the *E. coli* cell wall, ignoring its hemispherical endcaps. It is convenient to use the language of differential geometry in modeling differential growth. In general, geometric information about a surface, a subset of  $\mathbb{R}^3$  whose coordinates  $\vec{r}_i$  are functions of two independent parameters, can be encoded in a metric, a quantity which relates small increments in parameter space to the lengths of corresponding steps on the surface. The covariant metric tensor associated with any surface parameterization  $\vec{r}(x_1, x_2)$  is  $g_{ij} = \vec{m}_i \cdot \vec{m}_j$ , where  $\vec{m}_i = \partial \vec{r} / \partial x_i$ . A cylinder of radius  $r$  and length  $L$ , for instance, is parametrized in cylindrical coordinates ( $x \in [0, L], \theta \in [0, 2\pi]$ ) as  $\vec{r} = (x, r \sin \theta, r \cos \theta)$  and described by the metric tensor

$$(g_{ij}) = \begin{pmatrix} 1 & 0 \\ 0 & r^2 \end{pmatrix}. \quad (\text{S1})$$

The cylinder is not the only shape that possesses this metric: there can be many embeddings of this metric in  $\mathbb{R}^3$ . By Gauss's theorem egregium, any isometric embedding preserves the Gaussian curvature of the cylindrical metric and does not cause any elastic stretching of the two-dimensional material (but may be penalized by other factors, or extrinsic properties, that depend on the embedding and not the metric). An example of an extrinsic property is the mean curvature. The free energy of an elastic shell generally contains contributions due to both an in-plane stretching energy and a curvature energy which quadratically penalizes changes in mean curvature from the initial conformation. For extremely thin shells like the *E. coli* cell wall, the curvature energy is negligible compared to the stretching energy. Hence, it is valid to ignore the curvature energy and model the *E. coli* cell wall as an elastic membrane. Another extrinsic property which can change the embedding of the shell is an internal pressure, which is relevant to *E. coli* and will be discussed below.

**Differential growth of the bacterial cell wall.** We model the cell wall as an isotropic, homogeneous, linear-elastic membrane which is plastically deformed due to growth [1, 2]. There is evidence for cell wall growth occurring through circumferential insertions of glycan strands that are then crosslinked to their neighboring strands [3, 4, 5]. The insertion of glycan strands in the circumferential direction can be coupled to the mechanical strains and other elastic quantities of the cell wall, which may not assume a uniform profile. Generally, growth can be described as a flow on the metric [6, 7]: after sustained growth, the *target metric*  $g^t$  may be different from the *initial metric*  $g^b$ . The components of the target metric, which describes the intrinsic geometry of the cell after growth, can be arbitrary functions of the surface coordinates  $x_1$  and  $x_2$ :  $g_{ij}^t = g_{ij}^t(x_1, x_2)$ . The energetic penalty for deviating from this metric is the in-plane stretching energy

$$E_{\text{stretch}} = \frac{1}{2} \int u_{ij} \sigma_{ij} dx_1 dx_2, \quad (\text{S2})$$

where  $u_{ij} = U_i^j$  are the mixed (covariant and contravariant) forms of the strain tensor  $U = \frac{1}{2}(g - g^t)$ ,  $\sigma_{ij}$  are the associated stress resultants, and  $g$  is the metric of the actual embedding (which may differ from  $g^b$ ). Here, index lowering and raising are defined with respect to  $g^t$ . In the absence of extrinsic properties such as pressure, the realized embedding is simply the one which minimizes  $E_{\text{stretch}}$ . However, an internal pressure results in an additional pressure-volume term in the total energy

$$\mathcal{H} = -pV + E_{\text{stretch}}, \quad (\text{S3})$$

and may thus change the equilibrium embedding. Finding the equilibrium embedding for *E. coli* then becomes a more delicate problem, and we address this numerically below.

Generally, upon realizing the equilibrium embedding, a cell's shape may not be cylindrical. Determining the embedding may therefore yield information about past growth processes and patterns of glycan insertions. In addition to the final shape, any residual stresses may affect the subsequent growth of the cell. Both the shape due to a metric and the associated elastic quantities are therefore objects of interest in our theory.

**Target metric of a cell with uniform differential growth.** In this section, we find the target metric  $g^t$  for a growing *E. coli* cell subject to differential growth as a result of bending. This determines the form of  $E_{\text{stretch}}$ , which is needed to find the equilibrium embedding and stress profile.

We consider growth that is uniform along the cylinder length, meaning that if

$$g^t = \begin{pmatrix} g_{11}^b(1 + f_1(x, \theta))^2 & 0 \\ 0 & g_{22}^b(1 + f_2(x, \theta))^2 \end{pmatrix} = \begin{pmatrix} (1 + f_1(x, \theta))^2 & 0 \\ 0 & r^2(1 + f_2(x, \theta))^2 \end{pmatrix}, \quad (\text{S4})$$

where  $g^t$  is the target metric and  $g_{ij}^b$  are components of the initial, cylindrical metric, then  $f_1$  and  $f_2$  are functions of  $\theta$  alone that encode the geometric changes caused by the growth process. The condition that  $f_1$  and  $f_2$  are functions of  $\theta$  alone reflects our assumption that the differential growth is uniform over different cross-sections of the cell. We further postulate that differential growth acts in the direction of the long axis of the cell, so that  $f_2(\theta) = 0$ . This is the mode of growth if the PGEM adds new PG strands strictly along the circumference. We now determine the form of  $f_1(\theta)$ , which corresponds to growth that pushes apart points along the long axis, but not along the circumference.

We hypothesize that differential growth depends on the areal strain. The deformation of the cell, as it is confined in the microchamber, then determines the form of  $f_1(\theta)$ . The bending of a circular, cylindrical shell of radius  $r$  into a circular, toroidal shell results in a  $u_{xx}$  component of the form

$$u_{xx}^b \approx B \sin \theta, \quad (\text{S5})$$

a result that is familiar from Euler-Bernoulli beam theory. Here the superscript  $b$  denotes quantities induced by bending, and  $B$ , the *bending parameter*, is assumed small compared to unity and sets the curvature of the bent cylinder via  $R_{\text{curv}} = r/B$ , where  $R_{\text{curv}}$  is the major radius of the toroidal section (and hence the radius of the microchamber when the cell is confined). The strain tensor is expressed with respect to the surface coordinates  $(x, \theta)$ , where  $x = R_{\text{curv}}\phi$ ,  $\theta = y/r$ , and  $(\phi, \theta)$  are doubly polar coordinates.

Although we shall see that it is valid to ignore the cross-sectional ovalization due to bending in *E. coli*, it is also possible for the cell to react in the circumferential direction due to the Poisson effect so that  $\sigma_{yy}^b \approx 0$ . In confirmation of this, we numerically simulated a pressurized cylinder subjected to a bending moment using the finite-element software Abaqus FEA (Dassault Systems, Providence, RI). The simulation details are discussed in the Supplementary Methods. The results, which are summarized in Supplementary Fig. 1, suggest that  $\sigma_{xx}^b \approx YB \sin \theta$  and  $\sigma_{yy}^b \approx 0$ . Thus, from the Hookean constitutive relations for a linear-elastic material

$$u_{xx} = \frac{1}{Y}(\sigma_{xx} - \nu\sigma_{yy}), \quad u_{yy} = \frac{1}{Y}(\sigma_{yy} - \nu\sigma_{xx}), \quad (\text{S6})$$

we obtain  $u_{yy}^b = -\nu B \sin \theta$ .

From the strain tensor, it is easily seen that the areal strain  $A = (1 + u_{xx})(1 + u_{yy}) - 1$  caused by the deformation contains sinusoidal variations which are linear in  $B$ . We shall ignore the non-sinusoidal variations in  $A$ , which are higher-order in  $B$ . Consider now a growth rate which depends on the areal strain as described in the main text. For a pressurized bent cell, we anticipate that  $A \approx A_0 + A_1 \sin \theta$ , where the constant term is due to uniform stretching caused by pressure and the variational term comes from bending under microchamber confinement. If differential growth is proportional to the differential areal strain  $A_1 \sin \theta$ , then  $f_1(\theta) = c \sin \theta$ , where the coefficient  $c$  is set by the growth rates and the time of growth in the bent state. We call  $c$  the *differential growth parameter*, and relate  $c$  to  $A_1$  in Supplementary Note 2. The target metric prescribed by differential growth is then

$$g_{ij}^t = \begin{pmatrix} (1 + c \sin \theta)^2 & 0 \\ 0 & r^2 \end{pmatrix}, \quad (\text{S7})$$

which completely specifies the form of  $E_{\text{stretch}}$ . The equilibrium embedding and residual stresses in the presence of pressure are determined in the next section.

We finally return to the assumption that it is acceptable to ignore any cross-sectional ovalization caused by the longitudinal tension and compression which resist the applied bending moment. This ovalization is widely known as the *Brazier effect*, first studied by L. G. Brazier in 1927, and is responsible for the buckling behavior of cylindrical shells under bending [8]. However, in the presence of a large internal pressure which resists ovalization—as for the case of the *E. coli* cell wall—the cross-sectional eccentricity becomes vanishingly small. In particular, assuming that a typical cross-section deforms due to longitudinal tension and compression according to  $w = r\varepsilon \cos(2\theta)$ , where  $w$  is the radial component of displacement due to bending, we find

$$\varepsilon \approx \frac{Yt^2r^4}{t^2R_{\text{curv}}^2(Yt^2 + 4pr^3)} \approx \frac{Yr}{4R_{\text{curv}}^2p}, \quad (\text{S8})$$

where  $E$  is the three-dimensional elastic modulus,  $h$  is the thickness,  $\nu$  is the Poisson ratio of the shell,  $Y = Eh$ ,  $t = h(1 - \nu^2)^{-1/2}$ , and  $p$  is the internal pressure [9]. We see that  $\varepsilon$  is higher-order in  $B$ ; for characteristic values of  $h = 3$  nm,  $\nu = 1/3$ ,  $E = 30$  MPa,  $R_{\text{curv}} = 4$   $\mu\text{m}$ ,  $r = 0.5$   $\mu\text{m}$ , and  $p$  ranging from 0.3-2 atm (see Supplementary Table 1),  $\varepsilon = 0.004$ - $0.0234$ , which is small compared to  $B = r/R_{\text{curv}} = 0.125$  in our experiments. Interestingly, if *E. coli* were not internally pressurized, then the corresponding value of  $\varepsilon \approx 400$  surpasses the buckling limit of  $\varepsilon \approx 2/9$ , and the cell wall may have buckled inside the microchamber.

Note that the foregoing discussion applies only to the deformation of cylindrical shells under an applied bending moment. Although an internal pressure may intuitively resist cross-sectional deviations from a circle, this intuition is incorrect when considering the equilibrium of a pressurized torus of circular cross-section, as we do below. In particular, loading a circular torus with an internal pressure results in nontrivial cross-sectional deformations [10, 11].

**Numerical solution for a residually stressed cell.** Having determined the form of  $g^t$  in equation (S7), we now wish to determine the embedding and associated elastic quantities of the cell when released from the microchamber.

If the embedding of the cell were fully compatible with the target metric of equation (S7), then the cell wall may be parametrized by the surface  $\vec{r}(\phi, \theta) = ((R + r \sin \theta) \cos \phi, (R + r \sin \theta) \sin \phi, r \cos \theta)$ , which describes a circular toroid with major radius  $R = r/c$ . A direct calculation reveals that this parameterization has a metric tensor exactly matching that of equation (S7), and would be the embedding describing the cell wall if the pressure were small enough so that  $pV \ll E_{\text{stretch}}$  and the total energy is  $\mathcal{H} \approx E_{\text{stretch}}$ . The stress resultants of a circular torus loaded by an internal pressure  $p$  are, in surface coordinates  $(x, y) = (R\phi, r\theta)$ ,

$$\sigma_{xx} = \frac{pr}{2}, \quad \sigma_{yy} = \frac{pr}{2} \left( \frac{2 + c \sin \theta}{1 + c \sin \theta} \right). \quad (\text{S9})$$

This result assumes geometric linearity—namely, that pressure loading does not change the embedding  $\vec{r}$ —and results in an infinite displacement field at the crowns [12]. A solution which corrects for the latter involves a boundary layer analysis or detailed examination of geometric nonlinearity [10, 11]. In this work, we will not concern ourselves with this more detailed analysis.

Because equation (S9) assumes geometric linearity, it is not immediately applicable to the *E. coli* cell wall, which is under a large internal pressure and finitely strained. A large pressure may change the embedding that minimizes  $\mathcal{H}$ , resulting in geometric nonlinearity of the deformation gradient. Due to the path-independence of equilibrium states, we therefore consider the equivalent problem of loading a circular toroidal section with bending parameter  $c$  with a large internal pressure. This is a complicated problem for which an analytic, shell-theoretic solution is difficult. In order to explore whether or not a pressure of the same magnitude as *E. coli*'s turgor pressure may affect the embedding and thus the associated stress profile, we undertook numerical simulations using Abaqus FEA. The methodology is reviewed in the Sup-

plementary Methods; briefly, a capped toroidal section was initialized as a fine mesh and equilibrated with respect to a range of internal pressures. Although complicated, small-amplitude variations in  $\sigma_{xx}$  appear for large strains where  $pr/Y \approx 0.1$  (which is relevant to *E. coli*; see Supplementary Table 1), the numerical results are surprisingly well-approximated by the linear-theoretic stress profile of equation (S9) (Supplementary Figs. 2b-c).

We offer an interpretation of our numerical results, and in particular the lack of variation in  $\sigma_{xx}$ , by noting that there is negligible torque due to pressure for shells with circular cross-sections [1]. This would imply that, even in the presence of a large pressure, a non-circular cross-section is necessary for variation in the axial stresses. To see this, we consider a shell under internal pressure as pictured in Supplementary Fig. 2a. The upper-half portion of the shell, which is cut by the shaded plane, is in mechanical equilibrium. The sum of all forces acting on the region must vanish by the condition of equilibrium. The contribution to the torque exerted on the shell by pressure around a point  $A$  is exactly that coming from the contour above, which by force balance is equivalent to the torque associated with the cross-section containing  $A$ . Since the center of mass of a circular cross-section coincides with the moment center, there is no lever arm and this torque must vanish. Thus, a shell with circular cross-section cannot have a variational axial stress component. Further analysis of a toroidal shell with elliptic cross-section indicates that a finite eccentricity can result in sinusoidal variations in  $\sigma_{xx}$  [13]. These remarks are consistent with our simulation results, where we observed typical cross-sections of the deformed geometry to have a vanishingly small eccentricity.

In summary, our numerical results suggest that it is valid to approximate the stress profile of a cell in Phase 2 of our experiments with the linear result of equation (S9). From this, we remark that there are approximately no differential axial stresses at equilibrium, and in particular, that a growth mechanism which solely detects the axial stresses  $\sigma_{xx}$ , as implicated in previous work [14, 15], may fail to account for the observed straightening. However, as shown below, the nonvanishing variation in  $\sigma_{yy}$  results in a nonzero variation in the areal strain. Because the sign of this variation is opposite from that of the variation inside the microchamber, a growth mechanism which detects areal strain would result in straightening.

**Nonuniform crosslinking and anisotropic elasticity cannot explain straightening.** A previously proposed mechanism for shape regulation in bacteria, which may induce residual stresses in the cell wall, is the nonuniform crosslinking of glycan strands (or cleavage of peptide bonds, which can be considered similarly) [16]. Crosslinking inhomogeneity along the circumferential direction would be relevant if the crosslinking machinery in *E. coli* preferentially linked glycan strands according to local density or area.

To probe whether or not nonuniform crosslinking of glycan strands also produces variations in elastic quantities that can explain the observed straightening, we modeled crosslinking inhomogeneity by taking the elastic modulus of the cell wall to vary azimuthally:  $Y(\theta) = Y(1 + d \sin \theta)$ , where  $d$  is a parameter quantifying the magnitude of the inhomogeneity and  $Y$  is again the two-dimensional elastic modulus of the cell, viewed as an isotropic material. Because a formal, shell-theoretic solution of the equilibrium state is difficult, we determined the equilibrium stress profile numerically with Abaqus FEA simulations (Supplementary Fig. 3). Interestingly, our simulation results reveal that both  $\sigma_{xx}$  and the areal strains are larger on the outer edge of the deformed state, where  $Y$  is *smaller*. The possibility of stress-dependent crosslinking explaining straightening can be ruled out from this “sign error” alone: if a smaller axial stress or areal strain results in more crosslinking and an increased value of  $Y$  inside the microchamber, then upon release there would be a runaway effect with no straightening. If a larger axial stress or areal strain leads to more crosslinking, then the snapback in the microfluidics experiment discussed in the main text should have been in the direction opposite the applied flow [1]. We thus conclude that growth which localizes to the axial stresses or areal strains incurred by nonuniform crosslinking cannot explain our straightening observations.

Although we have modeled the *E. coli* cell wall as an isotropic shell described by two elastic constants ( $E, \nu$ ), there is also evidence that PG is stiffer in the circumferential direction than the axial direction due to the circumferential orientation of glycan strands [17, 18]. To probe whether cell wall anisotropy can lead to substantial variations in elastic quantities, we performed Abaqus FEA simulations in lieu of more complicated,

anisotropic elasticity calculations. We simulated an orthotropic half-toroidal shell with a circumferential elastic modulus twice as large as the axial one under internal pressure; this takes into account both the effects of differential growth and anisotropic elasticity. Our results, which are summarized in Supplementary Fig. 4, show small, non-sinusoidal variations in  $\sigma_{xx}$  and nearly identical variations in  $\sigma_{yy}$  compared to the differential growth case. Thus, although a more accurate model of cell wall elasticity may involve it, anisotropic elasticity is insufficient to explain our observations: it does not result in the form of  $\sigma_{xx}$  necessary for an axial stress-dependent growth rate to explain our straightening observations; neither does it yield larger variations in  $\sigma_{yy}$  than can be obtained simply by considering differential growth alone.

**Elastic quantities for a cell inside and outside the microchamber.** In order to model the coupling of growth to areal strains in the cell wall, we require the form of the areal strains both inside and outside the microchamber. The stress profile of a straight cylinder, i.e. that of the cell in the undeformed state, is  $\sigma_{xx} = pr/2$  and  $\sigma_{yy} = pr$ . By linear superposition of strains, the strain profile of a bent cell inside the microchamber is (c.f. equation (S5))

$$u_{xx}^{in} \approx \eta \left( \frac{1}{2} - \nu \right) + (B - c) \sin \theta, \quad u_{yy}^{in} = \eta \left( 1 - \frac{\nu}{2} \right) - \nu(B - c) \sin \theta, \quad (\text{S10})$$

where we have set  $\eta = pr/Y$  and anticipate  $\eta$ , a dimensionless pressure, to be of order unity in our experiments [14]. Note that the  $-c \sin \theta$  term arises from differential growth and adaptation of the cell to the bending force inside in microchamber. In particular, the differential growth parameter offsets the degree of bending, and the deformation can be viewed as one from a torus with bending parameter  $c$  to a torus with a bending parameter  $B$ .

We now recall the linear theory approximation to the residual stresses caused by differential growth:

$$\sigma_{xx}^{out} \approx \frac{pr}{2}, \quad \sigma_{yy}^{out} \approx \frac{pr}{2} \left( \frac{2 + c \sin \theta}{1 + c \sin \theta} \right) \approx pr - \frac{prc}{2} \sin \theta. \quad (\text{S11})$$

To first order in  $c$ , the areal strains  $A = (1 + u_{xx})(1 + u_{yy}) - 1$  both inside and outside the microchamber are

$$A^{in} = A_0^{in} + \delta A^{in} \approx \frac{6\eta + 2\eta^2 - 6\eta\nu - 5\eta^2\nu + 2\eta^2\nu^2}{4} + (1 + \eta - \nu - \eta\nu + \eta\nu^2) (B - c) \sin \theta, \quad (\text{S12})$$

$$A^{out} = A_0^{out} + \delta A^{out} \approx \frac{6\eta + 2\eta^2 - 6\eta\nu - 5\eta^2\nu + 2\eta^2\nu^2}{4} - \frac{c\eta}{4} (2 - 2\nu + \eta - 4\eta\nu + \eta\nu^2) \sin \theta. \quad (\text{S13})$$

Henceforth we will replace the “ $\approx$ ” symbol with “=” in equations (S12) and (S13) to avoid confusion with subsequent approximations.

If the quantity  $B - c$  is positive inside the microchamber, meaning that the differential growth relieves some but not all of the areal strain incurred by bending, then the variational terms  $\delta A^{in}$  and  $\delta A^{out}$  are opposite in sign inside and outside the microchamber for a broad range of material parameters relevant to *E. coli* (as summarized in Supplementary Table 1). A growth rate that depends on areal strain may therefore qualitatively account for the observed straightening. We show in the following sections that it is quantitatively consistent with the straightening as well, with an areal strain-growth coupling parameter that can be inferred directly from the snapback event.

## Supplementary Note 2

We now derive equation (3) in the main text and show that areal strain-dependent initiation of new glycan strands, according to the form of the areal strains from equations (S12) and (S13), is quantitatively consistent with the experimentally observed straightening rate. Our consideration of the growth dynamics of an unconfined toroidal shell can be generalized to other geometries and may be useful for describing the growth of other surfaces [14, 15].

**Dynamics.** If the initiation rate of new glycan strands is areal strain-dependent, then the growth at a given angle will depend on the initiations that happened at a different angle, with MreB decays being modeled as a Poisson process with rate  $1/\tau$ . Let  $k$  denote a constant, net rate of initiation per unit area. In a curved cell, the outer side of the cell is longer than the inner side, and thus the probability of initiation will be larger on the outer side of the cell if there is no strain-coupling. The infinitesimal surface area element on a small toroidal segment of radius  $r = R_{\text{cell}}$  and radius of curvature  $R_{\text{curv}}$  is

$$dA(\theta, t) = \left(1 + \frac{r}{R_{\text{curv}}} \sin \theta\right) d\bar{L}r d\theta = (1 + B(t) \sin \theta) d\bar{L}(t)rd\theta, \quad (\text{S14})$$

where  $d\bar{L} = d\bar{L}(t)$  is the infinitesimal width of the segment averaged over the cross-section at a time  $t$ , which is identical to the length along the midline. If the number of glycan strand initiations  $\gamma$  per unit area can be linearly decomposed into strain-independent and strain-dependent components as  $\gamma(\theta, t) = k + \alpha\delta A(\theta, t)$ , where  $k$  is a constant, strain-independent rate,  $\delta A(\theta, t)$  is the variational areal strain as a function of angle  $\theta$  and time  $t$ , and the parameter  $\alpha$  quantifies the intensity of growth-strain coupling (c.f. equation (2) in the main text), then the probability of initiation between angles  $\theta$  and  $\theta + d\theta$  at time  $t$  is

$$p(\theta, t)d\theta = \gamma(\theta, t)(1 + B(t) \sin \theta)rd\theta = (k + \alpha\delta A(\theta, t))(1 + B(t) \sin \theta)rd\theta. \quad (\text{S15})$$

In fact, the form of  $\gamma$  may be more generally applicable: if  $f[\delta A(\theta, t)]$  is a functional that quantifies the variational areal strain coupling with an intensity parameter  $\beta$ , then expanding  $f$  to first order in  $\delta A$  gives the initiation rate  $\gamma$  as

$$\gamma(\theta, t) = k + \beta f[\delta A(\theta, t)] = k + \beta(f_0 + f_1\delta A(\theta, t)), \quad (\text{S16})$$

where  $f_0$  and  $f_1$  are constants. By aggregating the constant terms, we recover equation (S15) above.

Note that  $k$  includes the effect of PG turnover [19, 20] and can be expressed in terms of the new glycan strand initiation rate  $k_{\text{new}}$  and the degradation rate  $k_{\text{deg}}$  as  $k = k_{\text{new}} - k_{\text{deg}}$ . From the self-consistent expressions of  $k$  and  $\alpha$  determined below, we see that characteristic values of  $\alpha\delta A$  are smaller than  $k_{\text{new}}$  and the ratio  $|\alpha\delta A|/k_{\text{new}} \approx 30\text{-}70\%$  (as can be found using the parameter values given in Supplementary Table 1 and equations (S12) and (S13)). This suggests that strain-dependent initiation of new glycan strands is typically a moderate effect relative to the total initiation of new glycan strands.

Let  $\tau$  denote the persistence time of MreB and  $M = v/r$  its angular speed. Since MreB is assumed to degrade as a Poisson process with rate  $1/\tau$ , the amount of material added per initiation event by an MreB molecule going in the  $+\theta$  direction as a function of  $\theta$  is  $\Delta L_s(\theta) = L_0 e^{-\theta/M\tau}$ , where  $L_0$  is the width of one PG insert. The growth rate is given by convolving  $p$  and  $\Delta L_s$  over  $\theta$ , resulting in the integro-differential ‘‘growth’’ equation

$$\begin{aligned} \frac{1}{\bar{L}} \frac{\partial L}{\partial t} \Big|_{\theta} &\approx \frac{L_0 r}{2} \left( \int_{-\infty}^{\theta} d\theta' \gamma \left( \theta', t - \frac{\theta - \theta'}{M} \right) \left( 1 + B \left( t - \frac{\theta - \theta'}{M} \right) \sin \theta' \right) e^{-\frac{\theta - \theta'}{M\tau}} e^{-\frac{\theta - \theta'}{M} \lambda} \right. \\ &\quad \left. + \int_{\theta}^{\infty} d\theta' \gamma \left( \theta', t + \frac{\theta - \theta'}{M} \right) \left( 1 + B \left( t + \frac{\theta - \theta'}{M} \right) \sin \theta' \right) e^{\frac{\theta - \theta'}{M\tau}} e^{\frac{\theta - \theta'}{M} \lambda} \right), \end{aligned} \quad (\text{S17})$$

where the second integral is the result of taking MreB molecules moving in the opposite  $-\theta$  direction ( $M \mapsto$

$-M$  and  $[-\infty, \theta] \mapsto [\theta, \infty]$ ) and we summarize the notation as follows:

$L = L(\theta, t)$  is the pole-to-pole length of the cell at angle  $\theta$  and time  $t$ ;  
 $\bar{L}$  is the *average* length over angles  $\theta$ , which is identical to the length of the midline;  
 $L_0$  is the width of one PG insertion;  
 $r$  is the radius of the cell;  
 $\delta A(\theta, t)$  is the differential areal strain (dimensionless);  
 $\alpha$  is a parameter for the growth rate-areal strain coupling (units of  $1/(\text{area}\cdot\text{time})$ );  
 $k$  is a constant initiation rate per area (units of  $1/(\text{area}\cdot\text{time})$ );  
 $M$  is the circumferential speed of MreB (units of radians/time);  
 $\tau$  is the persistence time of MreB;  
 $\lambda$  is the normalized growth rate of the cell, equivalent to  $d\bar{L}/(\bar{L}dt)$ ;  
 $c = c(t)$  is the differential growth parameter of the cell; and  
 $B = B(t)$  is the bending parameter of the cell.

(A full summary of all the persistent notation used in this work appears in Supplementary Table 1.) Note that equation (S17) is an approximation, as for simplicity we have taken the limits of integration to  $\mp\infty$  instead of bounding them. This approximation is supported for the parameter values tabulated in Supplementary Table 1 by simulations of the discrete growth process, as detailed in the Supplementary Methods (see also Supplementary Fig. 5 and Supplementary Video 11). To avoid confusion with subsequent approximations, we will again replace the “ $\approx$ ” symbol with “ $=$ ” in equation (S17).

In the growth equation (S17), the  $\exp(\pm\lambda|\theta - \theta'|/M)$  factors come from the identity  $\bar{L}(t_0) = \bar{L}(0) \exp(\lambda t_0)$ : the initiation of growth sites in the past not only depends on the strain profile in the past, but also the length (and curvature) of the cell in the past. Noting that  $\lambda$  sets a timescale and the processivity  $M\tau$  sets the scale for angles, it is clear that the rate  $k \sim \lambda/L_0 r M\tau$ . We now find the exact, self-consistent expression for  $k$  by considering growth without areal strain-coupling.

**Differential growth and straightening with no strain-coupling.** If the areal strain-growth coupling parameter  $\alpha = 0$ , then the length profile  $L$  in this case satisfies

$$\begin{aligned}
 \frac{1}{\bar{L}} \frac{\partial L}{\partial t} &= \frac{L_0 r}{2} \left( \int_{-\infty}^{\theta} d\theta' k \left( 1 + B \left( t - \frac{\theta - \theta'}{M} \right) \sin \theta' \right) e^{-\frac{\theta - \theta'}{M\tau}} e^{-\frac{\theta - \theta'}{M} \lambda} \right. \\
 &\quad \left. + \int_{\theta}^{\infty} d\theta' k \left( 1 + B \left( t + \frac{\theta - \theta'}{M} \right) \sin \theta' \right) e^{\frac{\theta - \theta'}{M\tau}} e^{\frac{\theta - \theta'}{M} \lambda} \right) \\
 &= \frac{k L_0 r M \tau}{1 + \lambda \tau} \left( 1 + \frac{(1 + \lambda \tau)(1 + \lambda \tau(1 - S))}{(1 + \lambda \tau(1 - S))^2 + (M\tau)^2} B(t) \sin \theta \right),
 \end{aligned} \tag{S18}$$

where we assume the ansatz  $B(t) = B_0 \exp(-\lambda S t)$  and, as in a previous work, define  $S$  as the *straightening coefficient* [16]. A differential growth  $f_1(\theta, t) = c(t) \sin \theta$  multiplies the average length  $\bar{L}(t) = \bar{L}(0) \exp(\lambda t)$  by a factor  $1 + c(t) \sin \theta$  along the  $x$ -direction:  $L(\theta, t) = \bar{L}(t)(1 + c(t) \sin \theta)$ , where we also identify  $c(t) = B(t)$  once the cell has equilibrated. For self-consistency, we require the expression in equation (S18) to equal

$$\frac{1}{\bar{L}} \frac{\partial L}{\partial t} = \frac{1}{\bar{L}(t)} \frac{\partial(\bar{L}(t)(1 + B(t) \sin \theta))}{\partial t} = \lambda(1 + (1 - S)B(t) \sin \theta). \tag{S19}$$

(Note that we assume, in interpreting the results of our MreB experiments in Fig. 5 of the main text, that MreB density is proportional to  $\frac{1}{L} \frac{\partial L}{\partial t}$  in this equation.) We thus see that

$$k = \frac{\lambda(1 + \lambda \tau)}{M\tau L_0 r} \quad \text{and} \quad 1 - S = \frac{(1 + \lambda \tau)(1 + \lambda \tau(1 - S))}{(1 + \lambda \tau(1 - S))^2 + (M\tau)^2}. \tag{S20}$$

The straightening coefficient is self-consistently described by a solution to a cubic equation. Equation (S20) differs from the corresponding expressions

$$k = \frac{\lambda}{M\tau L_0 r} \quad \text{and} \quad S = \frac{(M\tau)^2}{1 + (M\tau)^2} \quad (\text{S21})$$

in [16], where the authors assumed that  $\lambda\tau \ll 1$  and set  $B(t) = r/R_{\text{CURV}}$ ; namely, in [16], corrections to the area element due to length contraction and the decay of curvature  $B(t) = B_0 \exp(-\lambda St)$  were neglected. Neglecting these corrections can be useful for gaining intuition, as instead of the cubic equation for  $S$ , we obtain the simple form of equation (S21). In general, due to the coupling between straightening and area-dependent initiation, equation (S20) and not equation (S21) yields the correct expression for  $S$ . However, in the limit that  $M\tau \rightarrow \infty$ , both equation (S20) and equation (S21) yield  $S \rightarrow 1$ . In the limit that  $M\tau \rightarrow 0$  and  $\lambda\tau \ll 1$ , both equations also yield  $S \rightarrow 0$ .

Thus, both expressions for  $S$  result in a similar picture: assuming that  $\lambda\tau \ll 1$ , which is consistent with the parameter values in Supplementary Table 1, proportional growth is recovered in the zero processivity case  $M\tau = 0$ , where  $S = 0$  and  $B(t) = B_0$ . The infinite processivity case is recovered by taking  $S \rightarrow 1$ , so that  $B(t) = B_0 \exp(-\lambda t)$ . In the limit of high processivity with no strain-coupling, the bending parameter  $B(t)$  therefore decays exponentially with the growth rate, agreeing with the result in [16]. In summary, without strain-coupling the cell straightens as

$$B(t) \sim \begin{cases} \text{const.} & \text{zero processivity, no strain-coupling; no straightening} \\ \exp(-\lambda t) & \text{infinite processivity, no strain-coupling; straightening rate equals growth rate.} \end{cases} \quad (\text{S22})$$

We note again that the latter case, in which the straightening rate equals the growth rate, leads to self-similarity and not actual ‘‘straightening.’’ In particular, the *aspect ratio*  $L(t)B(t)$  does not decay with time.

**Small processivity with strain-coupling.** If the areal strain-coupling parameter  $\alpha$  does not vanish, then the growth equation assumes the full form of equation (S17):

$$\begin{aligned} \frac{1}{L} \frac{\partial L}{\partial t} \Big|_{\theta} &= \frac{L_0 r}{2} \left( \int_{-\infty}^{\theta} d\theta' \gamma \left( \theta', t - \frac{\theta - \theta'}{M} \right) \left( 1 + B \left( t - \frac{\theta - \theta'}{M} \right) \sin \theta' \right) e^{-\frac{\theta - \theta'}{M\tau}} e^{-\frac{\theta - \theta'}{M} \lambda} \right. \\ &\quad \left. + \int_{\theta}^{\infty} d\theta' \gamma \left( \theta', t + \frac{\theta - \theta'}{M} \right) \left( 1 + B \left( t + \frac{\theta - \theta'}{M} \right) \sin \theta' \right) e^{\frac{\theta - \theta'}{M\tau}} e^{\frac{\theta - \theta'}{M} \lambda} \right), \end{aligned} \quad (\text{S23})$$

where

$$\gamma(\theta, t) = \frac{\lambda(1 + \lambda\tau)}{L_0 r M\tau} + \alpha \delta A(\theta, t). \quad (\text{S24})$$

Evaluating equation (S23) gives

$$\frac{1}{L} \frac{\partial L}{\partial t} \Big|_{\theta} = \lambda(1 + (1 - S)B(t) \sin \theta) + J, \quad (\text{S25})$$

where

$$\begin{aligned} J &= \frac{L_0 r}{2} \left( \int_{-\infty}^{\theta} d\theta' \alpha \delta A \left( \theta', t - \frac{\theta - \theta'}{M} \right) \left( 1 + B \left( t - \frac{\theta - \theta'}{M} \right) \sin \theta' \right) e^{-\frac{\theta - \theta'}{M\tau}} e^{-\frac{\theta - \theta'}{M} \lambda} \right. \\ &\quad \left. + \int_{\theta}^{\infty} d\theta' \alpha \delta A \left( \theta', t + \frac{\theta - \theta'}{M} \right) \left( 1 + B \left( t + \frac{\theta - \theta'}{M} \right) \sin \theta' \right) e^{\frac{\theta - \theta'}{M\tau}} e^{\frac{\theta - \theta'}{M} \lambda} \right) \end{aligned} \quad (\text{S26})$$

is nonnegative and describes the contribution of strain-coupling to straightening. Here the ‘‘straightening coefficient’’  $S$  no longer appears in the expression for  $B(t)$ , but is a variable that conveniently satisfies an

equation analogous to equation (S20):

$$1 - S = \frac{(1 + \lambda\tau)(1 + \lambda\tau - \mu\tau)}{(1 + \lambda\tau - \mu\tau)^2 + (M\tau)^2}, \quad (\text{S27})$$

for  $B(t) = B_0 \exp(-\mu t)$ . We leave  $J$  unevaluated for now and focus instead on the growth *inside* the microchamber.

For the cell to grow at a constant differential growth  $c^0$  inside the microchamber under a constant strain-coupling parameter  $\alpha$ , a self-consistency criterion must be satisfied. In particular, considering the growth profile within the microchamber gives us an equation relating the constant differential growth  $c^0$  within the microchamber to the strain-coupling parameter  $\alpha$ . Inside the microchamber, the cell is subject to an areal strain of the form of equation (S12), which is proportional to the constant bending parameter  $B^0$  and relieved by a constant, self-consistent value of the differential growth parameter  $c^0$ . For the sign of the differential growth to be consistent with that of the differential areal strains, we require  $B^0 \geq c^0$ . The differential areal strain profile of the cell inside the microchamber, as given by equation (S12), is

$$\delta A(\theta, t) = (1 + \eta - \nu - \eta\nu + \eta\nu^2) (B^0 - c^0) \sin \theta. \quad (\text{S28})$$

We demand the differential growth to be at a steady state in the microchamber so that  $dc(t)/dt = 0$  and, from equation (S19), write

$$\lambda(1 + c^0 \sin \theta) \approx \lambda(1 + (1 - S)B^0 \sin \theta) + J_1, \quad (\text{S29})$$

where  $J_1 \propto \alpha(B^0 - c^0) \sin \theta$  is defined analogously to  $J$  but with the differential areal strain  $\delta A(\theta, t)$  *inside* the microchamber as shown in equation (S28). Note additionally that  $J_1$  is nonnegative. In the limit of small processivity and assuming that  $\lambda\tau, \mu\tau \ll 1$ ,  $S \rightarrow 0$  and equation (S29) reduces to

$$(c^0 - B^0) \sin \theta = J_1 \propto \alpha(B^0 - c^0) \sin \theta. \quad (\text{S30})$$

Thus, the only physical, self-consistent solution (with  $\alpha \geq 0$ ) for  $c^0$  is that the cell is differentially strain-free, i.e.  $B^0 = c^0$ . In this case, when the cell is released from the microchamber, there would be no snapback because the microchamber bending parameter  $B^0$  and the differential growth  $c^0$  are equal; the cell has adapted completely to the shape of the microchamber. Since we have found a nonvanishing elastic snapback in our experiments, we conclude that the case of small processivity with strain-coupling is inconsistent with the PG synthesis machinery in *E. coli*.

**Large processivity with strain-coupling.** Parameter values suggest that large processivity is relevant to MreB: assuming a persistence time of  $\tau = 5$  mins and a spot velocity of  $v = 5$  nm/sec [3, 21, 22], the processivity, in units of length, is  $M\tau r = 1.5\mu\text{m}$  where  $M = v/r = 0.01$  rad/sec and the cell radius  $r = 0.5\mu\text{m}$ . For  $\lambda\tau, \mu\tau \ll 1$ , this corresponds to a straightening coefficient of  $S = 0.9$ . For these large processivities, the growth due to coupling to areal strain is given again by equation (S23). Temporarily ignoring the constant terms in the integrands and taking the zeroth-order term in  $B(t)$ , the relevant integrals describing the growth *after release from the microchamber* are proportional to

$$\int_{-\infty}^{\theta} d\theta' c \left( t - \frac{\theta - \theta'}{M} \right) e^{-\frac{\theta - \theta'}{M\tau}} e^{-\frac{\theta - \theta'}{M}\lambda} \sin \theta' + \int_{\theta}^{\infty} d\theta' c \left( t + \frac{\theta - \theta'}{M} \right) e^{\frac{\theta - \theta'}{M\tau}} e^{\frac{\theta - \theta'}{M}\lambda} \sin \theta'. \quad (\text{S31})$$

We therefore need to specify the form of  $c(t)$ . Taking  $t = 0$  to be the time when the cell is released from the microchamber, we assume an ansatz for  $c(t)$  of the form

$$c(t) = \begin{cases} c^0 \exp(-\mu t) & t \geq 0 \\ c^0 & t < 0 \end{cases} \quad (\text{S32})$$

and, to be precise, bound the limits of integration so that we integrate starting from a time  $t_0 = t + t_c$  in the

past, where  $t_0 \rightarrow \infty$  is the total time the cell has been in existence (i.e., the sum of both the confined time  $t_c$  and released time  $t$  from the microchamber). We recall that the differential areal strain profile is

$$\delta A(\theta, t) = \begin{cases} -\frac{c\eta}{4}(2 - 2\nu + \eta - 4\eta\nu + \eta\nu^2) \sin \theta \equiv \xi_1 c \sin \theta & t \geq 0 \\ (1 + \eta - \nu - \eta\nu + \eta\nu^2)(B^0 - c) \sin \theta \equiv \xi_0(B^0 - c) \sin \theta & t < 0, \end{cases} \quad (\text{S33})$$

where we have defined  $\xi_0$  and  $\xi_1$  so that  $\xi_0 > 0$  and  $\xi_1 < 0$  for the parameter values listed in Supplementary Table 1. Thus, neglecting terms in the integrand of equation (S23) which are of order  $B^2$ , we have

$$\frac{1}{\bar{L}} \frac{\partial L}{\partial t} \Big|_{\theta} = \lambda(1 + (1 - S)B(t) \sin \theta) + \frac{L_0 r}{2}(I_1 + I_2), \quad (\text{S34})$$

where  $I_1$  and  $I_2$  are defined as the integrals

$$\begin{aligned} I_1 &= \alpha \xi_0 (B^0 - c^0) \int_{\theta - Mt_0}^{\theta - Mt} d\theta' e^{-\frac{\theta - \theta'}{M\tau}} e^{-\frac{\theta - \theta'}{M}\lambda} \sin \theta' \\ &\quad + \alpha \xi_1 \int_{\theta - Mt}^{\theta} d\theta' c \left( t - \frac{\theta - \theta'}{M} \right) e^{-\frac{\theta - \theta'}{M\tau}} e^{-\frac{\theta - \theta'}{M}\lambda} \sin \theta', \end{aligned} \quad (\text{S35})$$

$$\begin{aligned} I_2 &= \alpha \xi_0 (B^0 - c^0) \int_{\theta + Mt}^{\theta + Mt_0} d\theta' e^{\frac{\theta - \theta'}{M\tau}} e^{\frac{\theta - \theta'}{M}\lambda} \sin \theta' \\ &\quad + \alpha \xi_1 \int_{\theta}^{\theta + Mt} d\theta' c \left( t + \frac{\theta - \theta'}{M} \right) e^{\frac{\theta - \theta'}{M\tau}} e^{\frac{\theta - \theta'}{M}\lambda} \sin \theta'. \end{aligned} \quad (\text{S36})$$

This is the same calculation as the small processivity case with  $J = I_1 + I_2$ ; however, we now desire to evaluate these integrals explicitly. Doing so, we find

$$I_1 + I_2 = \alpha \xi_0 (B^0 - c^0) \Psi_1 \sin \theta + \alpha \xi_1 \Psi_2 \sin \theta, \quad (\text{S37})$$

where

$$\Psi_1 = \frac{2M\tau(e^{-(\lambda+1/\tau)t}((1 + \lambda\tau) \cos(Mt) - M\tau \sin(Mt)) + e^{-(\lambda+1/\tau)t_0}(-(1 + \lambda\tau) \cos(Mt_0) + M\tau \sin(Mt_0)))}{(1 + \lambda\tau)^2 + (M\tau)^2} \quad (\text{S38})$$

and

$$\Psi_2 = \frac{2c^0 M\tau(e^{-\mu t}(1 - \mu\tau + \lambda\tau) - e^{-(\lambda+1/\tau)t}(1 - \mu\tau + \lambda\tau) \cos(Mt) + M\tau e^{-(\lambda+1/\tau)t} \sin(Mt))}{1 - 2\mu\tau + 2\lambda\tau + (\mu\tau)^2 - 2\mu\lambda\tau^2 + (\lambda\tau)^2 + (M\tau)^2}. \quad (\text{S39})$$

The expression for  $I_1 + I_2$  contains oscillations that decay as  $\exp(-(\lambda+1/\tau)t)$ .  $1/\tau$  is a rate that is larger than the growth rate in our experiments: as  $t_d \approx 30$  min, the MreB persistence time  $\tau \approx t_d/6$ . Since biological parameter values suggest that it is valid to assume  $1/\tau \gg \mu \geq \lambda$ , i.e. that the persistence time of MreB is smaller than the doubling time of the cell (see also Supplementary Table 1), we can take the  $e^{-(\lambda+1/\tau)t} \cos(Mt)$  and  $e^{-(\lambda+1/\tau)t} \sin(Mt)$  terms above to be small in comparison to  $e^{-\mu t}$ , and the  $e^{-(\lambda+1/\tau)t_0} \cos(Mt_0)$  and  $e^{-(\lambda+1/\tau)t_0} \sin(Mt_0)$  terms to vanish for large enough  $t_0$ . Thus we have

$$I \equiv I_1 + I_2 \approx \frac{2\alpha \xi_1 c^0 M\tau e^{-\mu t} (1 - \mu\tau + \lambda\tau) \sin \theta}{1 - 2\mu\tau + 2\lambda\tau + (\mu\tau)^2 - 2\mu\lambda\tau^2 + (\lambda\tau)^2 + (M\tau)^2}. \quad (\text{S40})$$

We then impose the self-consistency criterion from equation (S19), which describes the action of the differential growth  $c$  on the length  $\bar{L}$ :

$$\frac{dc(t)}{dt} \sin \theta + \lambda(1 + c(t) \sin \theta) = \lambda(1 + (1 - S)B(t) \sin \theta) + \frac{L_0 r}{2} I. \quad (\text{S41})$$

Note additionally that  $S \rightarrow 1$  in the infinite processivity limit. Equation (S41) then becomes a cubic equation for  $\mu$  which can be solved numerically. However, to first find the value of  $c^0$  that gives a self-consistent differential growth profile within the microchamber, we again demand the differential growth to be at a steady state in the microchamber, so that  $dc(t)/dt = 0$  for  $t < 0$  and, for the confined differential areal strain profile  $\delta A(\theta, t) = \xi_0(B^0 - c^0) \sin \theta$ ,

$$\begin{aligned} \lambda c^0 \sin \theta &= \frac{L_0 r}{2} \left( \alpha \xi_0 (B^0 - c^0) \int_{\theta - Mt_c}^{\theta} d\theta' e^{-\frac{\theta - \theta'}{M\tau}} e^{-\frac{\theta - \theta'}{M}} \lambda \sin \theta' \right. \\ &\quad \left. + \alpha \xi_0 (B^0 - c^0) \int_{\theta}^{\theta + Mt_c} d\theta' e^{\frac{\theta - \theta'}{M\tau}} e^{\frac{\theta - \theta'}{M}} \lambda \sin \theta' \right) \\ &\approx \frac{\alpha \xi_0 (B^0 - c^0) L_0 r M \tau \sin \theta}{(1 + \lambda \tau)^2 + (M\tau)^2} \left( (1 + \lambda \tau) - e^{-(\lambda + 1/\tau)t_c} \left( (1 + \lambda \tau) \cos(Mt_c) - M\tau \sin(Mt_c) \right) \right), \end{aligned} \quad (\text{S42})$$

where the cell has been inside the microchamber for a time  $t_c$ , which is the same as the time the cell has been in existence (and assumed to be large). Thus, the constant differential growth inside the microchamber is given by

$$c_0 \approx \frac{\alpha B^0 L_0 r M \tau \xi_0}{\lambda + \lambda M^2 \tau^2 + \alpha L_0 r M \tau \xi_0} \approx \frac{\alpha B^0 L_0 r \xi_0}{\lambda M \tau + \alpha L_0 r \xi_0}, \quad (\text{S43})$$

where we again ignore the oscillations that decay as  $-t_c/\tau$  by assuming that the persistence time of the MreB is small compared to the doubling time,  $1/\tau \gg \mu \geq \lambda$ , and that  $t_c$  is large. The second approximation uses the assumption of large processivity,  $M\tau \gg 1$ .

To relate the straightening rate  $\mu$  to the snapback ratio  $\kappa$ , we note that, when the cell is removed from the microchamber, it elastically snaps to a bent cylinder described by the bending parameter  $B_{\text{snapback}} = c^0$ . Thus,  $\kappa$  is related to  $c^0$  as

$$\kappa = \frac{B_{\text{snapback}}}{B^0} = \frac{c^0}{B^0} \implies c^0 = B^0 \kappa. \quad (\text{S44})$$

For our theory of areal strain-dependent differential growth to be self-consistent, we require  $B^0 \geq c^0$ , or  $\kappa \leq 1$ , which agrees with our experimental observations. We may now solve equation (S41) for  $\mu$  to get the straightening enhancement in terms of  $\kappa$  and related parameters.

**Large processivity: approximating the straightening rate.** Supposing that  $M\tau \gg 1 \gg \mu\tau > \lambda\tau$ , the integral  $I$  in equation (S40) assumes the form

$$I \approx \frac{2\alpha \xi_1 c^0 e^{-\mu t} \sin \theta}{M\tau}. \quad (\text{S45})$$

Then equation (S41) reads, for  $c(t) = c^0 \exp(-\mu t)$ ,

$$\frac{dc(t)}{dt} \sin \theta + \lambda c(t) \sin \theta = (-c^0 \mu e^{-\mu t} + \lambda c^0 e^{-\mu t}) \sin \theta = \frac{L_0 r}{2} I. \quad (\text{S46})$$

Thus

$$\mu \approx \lambda - \frac{\alpha \xi_1 L_0 r}{M\tau}, \quad (\text{S47})$$

where we recall that  $\xi_1 < 0$ . Similarly, if  $M\tau \gg 1 \gg \mu\tau > \lambda\tau$ , from equation (S43) we have

$$c_0 \approx \frac{\alpha B^0 L_0 r \xi_0}{\lambda M \tau + \alpha L_0 r \xi_0}, \quad (\text{S48})$$

which also leads to an expression for the areal strain-growth coupling parameter  $\alpha$  in terms of the snapback ratio  $\kappa$  as

$$\alpha \approx \frac{c^0 M \lambda \tau}{L_0 r \xi_0 (B^0 - c^0)} = \frac{\kappa M \lambda \tau}{L_0 r \xi_0 (1 - \kappa)}. \quad (\text{S49})$$

Substituting equation (S49) into equation (S47), we have

$$\mu \approx \lambda \left( 1 - \frac{\kappa \xi_1}{(1 - \kappa) \xi_0} \right). \quad (\text{S50})$$

This approximation agrees well with numerical solutions of the full equation (S23) above, which are shown in Fig. 3 of the main text and Supplementary Fig. 6a. The methodology of the numerical analysis is described in the Methods section of the main text.

**Infinite MreB persistence and non-monotonicity of the straightening rate.** If  $\tau \rightarrow \infty$  but we do not assume that  $1/\tau \gg \lambda$ , then MreB can persist longer than the doubling time of the cell, and the  $e^{-(\lambda+1/\tau)t}$  terms cannot be neglected in equation (S37). A numerical solution of equation (S23) then shows that this leads to more oscillations, but a lower averaged straightening rate compared to the case of an intermediate processivity. For the parameter values summarized in Supplementary Table 1, Supplementary Fig. 6 shows a numerical solution of equation (S23) in both the regimes  $\tau : M\tau \gg 1 \gg \mu\tau > \lambda\tau$  and  $\tau : M\tau \gg \mu\tau > \lambda\tau > 1$ , which numerically confirms the existence of curvature oscillations in the latter case.

As discussed in the main text, the straightening rate  $\mu$  is non-monotone in the processivity  $\tau$  (measured in units of time, assuming a constant angular speed  $M$ ). Indeed, although straightening arises from the differential initiation of new glycan strands, previous growth sites can still be active and “wash away” the effect of areal strain-dependent initiation. We may quantify the non-monotonicity of  $\mu$  by solving equation (S41)—which holds for any processivity—without assuming either the limit of zero or infinite processivity. For simplicity, however, we consider only a finite range of  $\tau$  where  $1/\tau \gg \mu \geq \lambda$ , so that equation (S40) is still valid. Additionally, inside the microchamber, equation (S42) is modified to become

$$\lambda c^0 \sin \theta - \lambda(1 - S)B^0 \sin \theta \approx \frac{\alpha \xi_0 (B^0 - c^0) L_0 r M \tau \sin \theta}{1 + (M\tau)^2}. \quad (\text{S51})$$

The corrected form of the differential growth  $c^0$  is therefore related to the strain-coupling parameter  $\alpha$  as

$$\alpha = \frac{\lambda(c^0 - (1 - S)B^0)(1 + (M\tau)^2)}{L_0 r M \tau \xi_0 (B^0 - c^0)}. \quad (\text{S52})$$

The second equation is only valid if  $\alpha \geq 0$ , and in particular  $c^0 \geq (1 - S)B^0$ ; otherwise the choice of processivity is inconsistent with the observation of an elastic snapback, and the self-consistent solution requires the cell to be differentially strain-free as in the zero processivity case. With these corrections, equation (S41) is a cubic equation in  $\mu$  that can be numerically solved as a function of  $\tau$  when  $1/\tau \gg \mu \geq \lambda$ . The resulting numerical solution of  $\mu$ , which is non-monotone in  $\tau$ , is plotted over the domain  $\tau \in [1 \text{ min}, 50 \text{ min}]$  in Fig. 3d of the main text and compared to the quantity  $\lambda S(\tau)$ , where  $S(\tau)$  is numerically found by solving equation (S20) for the values of  $M$  and  $\lambda$  tabulated in Supplementary Table 1 and describes the straightening rate in the case of growth without areal strain-coupling. This calculation also allowed us to verify the validity of the approximation  $M\tau \gg 1$  used above, as we have assumed that, for MreB,  $M\tau = 3 \text{ rad}$  (Supplementary Table 1). For the range of parameter values considered in the main text, we found that the corrected values of  $\mu$  due to finite processivity deviate by less than 10% from the prediction of equation (S50).

## Supplementary Discussion

**Consistency with past microfluidics experiments.** In [1], one of us applied a hydrodynamic drag force on filamentous *E. coli* and *B. subtilis* cells and observed the deformation to induce both elastic bending and plastic remodeling of the cell wall. The deformed cells always recovered their straight, rod-like shape after growth, agreeing with the observations made in this study.

One detail that differs between the current experiment and the microfluidics setup is the degree of snapback observed by the cell upon equilibration. In [1], the authors observed characteristic snapback ratios of  $\kappa \approx 0.5$ , while we found  $\kappa = 0.78$  (see the Supplementary Methods). We can explain the discrepancy between these two observations by noticing that the areal strain profile incurred by the bending of a cell under a hydrodynamic drag force is nonuniform in the axial direction  $x$ . In particular, the cell has a nonuniform bending parameter  $B(x)$  along its length. Qualitatively, the differential initiation rate of such a cell would be smaller than the differential initiation rate of a cell bent uniformly by a bending parameter equal to the maximal value of  $B(x)$ . To reconcile these different snapback ratios quantitatively, we showed that they were consistent with each other under a common set of parameter values. Since a cell under hydrodynamic drag has complicated growth dynamics owing to the nonuniform stress profile, we performed MATLAB-based simulations of PG growth that numerically predicted the snapback in the experimental setup of [1]. We found several combinations of material parameter values and processivity values, in the range of those tabulated in Supplementary Table 1, that predicted both a snapback of  $\kappa \approx 0.5$  in [1] and a snapback of  $\kappa \approx 0.7$  in the current protocol. Furthermore, this check for self-consistency suggested a processivity of  $M\tau = 3$  to 6 radians and, assuming a constant spot velocity of  $v = 5$  nm/s, an MreB persistence time of  $\tau = 5$  to 10 minutes. This is consistent with the experimental value of  $\tau$  found in [23].

**Hyperosmotic shock during recovery.** For a large enough hyperosmotic shock, we expect the cellular turgor pressure to decrease and the straightening rate, which now depends on a smaller variational areal strain, to also decrease. We therefore verified that the cellular growth curves were similar during different degrees of osmotic shock (Supplementary Fig. 11a) and osmotically shocked cells with 100 mM and 250 mM LB+sorbitol solution upon release from the same microchamber environment in Phase 2. These osmotic shock magnitudes are believed to be sufficient to decrease the cellular turgor pressure by several atmospheres [24] and hence noticeably affect straightening. For 20-30 cells in each osmolarity, however, we found no evidence of osmotic shock affecting the straightening rate (Supplementary Fig. 11b). We attribute the absence of an effect on straightening to osmoregulation, which is believed to occur on a timescale  $\sim 1$  min [24, 25]. The fast timescale in which osmotic homeostasis occurs, relative to straightening, calls for more complex experimental protocols which can ascertain that the cellular turgor pressure is continually lowered over a timescale of  $\sim 30$  min.

## Supplementary Methods

**CurvatureTracker: a MATLAB-based software package for curvature analysis.** A summary of *CurvatureTracker*'s methodology can be found in the Methods section of the main text. Supplementary Fig. 7 shows an example of two image sequences involving the straightening of two distinct cells that were successfully tracked by *CurvatureTracker*.

Because the processed images have varying dimensions in pixels, we normalized all length quantities by the length (in pixels) of the cell in the first frame, and multiplied by the expected length at release,  $f\pi d$ , where  $f$  is the fraction of the microchamber the cell filled and  $d$  is the diameter of the microchamber, to obtain physical lengths.

In analyzing the straightening data with *CurvatureTracker*, we observed long tail behavior when the cell curvature was plotted as a function of time, which we believe to be indicative of substrate pinning or excessive growth whereby the cell became confined to the square microchamber and had insufficient space to straighten. We therefore truncated the dataset by discarding points over approximately 20 minutes ( $2/3$  the doubling time) of straightening and extracting the growth and straightening rates anew (Supplementary Fig. 8a). Because of the large density of data points at small times, we found that the corrected values differed only by less than 5%. For simplicity, we report all extracted values in our work using the full, untruncated time series. Below, we discuss the two different fits, local and global, that were used to describe the cell curvature.

**Image analysis methodology.** As a check on our experimental setup and *CurvatureTracker*, we checked that the normalized relative growth rate  $\lambda = dL/(Ldt)$  should be constant and positive, so that  $L(t) = L_0 \exp(\lambda t)$  (note that we have dropped the bar on the  $L$ , which denoted length along the midline). From the 60 processed image sequences, we extracted a mean value of

$$\lambda = 0.0416/\text{frame} = 0.0208 \text{ min}^{-1}. \quad (\text{S53})$$

This corresponds to a doubling time of  $\ln(2)/\lambda \approx 33$  min for *E. coli*, in agreement with the literature (around 30 minutes at 30°C [26, 27]; note also that the time between each imaged frame is 2 minutes). Similarly, if curvature decays exponentially as a function of time, then the relative decay rate over any interval  $X = [x_0, x_1]$  along the midline of the cell  $\mu(X) = -\partial C(X, t)/(C(X, t)\partial t)$ , where  $C(X, t)$  is the average curvature at segment  $X$  at time  $t$ , should be constant and positive so that  $C(X, t) = C_0(X) \exp(-\mu t)$ . We take  $X = [0.2, 0.8] \times (\text{cell length})$ , so that we consider the summed curvatures over the entire cell; in practice, the cell is divided into 10 ordered segments along its length and we average the absolute value of the curvature over segments 2 to 9. This method produced less noisy results as compared to computing the curvature over the lengths of entire cells, since the ends were free and oftentimes substantially more curved than the bulk of the cell. From the processed image stacks, we extracted a mean value of

$$\mu = 0.0752/\text{frame} = 0.0376 \text{ min}^{-1}, \quad (\text{S54})$$

which yields a straightening ratio of  $\mu/\lambda = 1.81$ . A plot of  $\ln(L/L_0)$  against  $\ln(C/C_0)$  for all processed stacks, which recapitulates the fits above and the faster-than-expected decay of curvature relative to infinite processivity, is shown in Supplementary Fig. 8a.

Because the cells were released from microchamber confinement when they filled approximately 90% of the circumference of the microchamber, which has a radius of 4  $\mu\text{m}$ , we used this length information to compute the average curvature at the frame  $t = 1$  to be  $C(X, 1) = 0.18 \mu\text{m}^{-1}$ . The initial curvature of this fit is then extrapolated as  $C(X, 0) = 0.18 \exp(\mu) \approx 0.194 \mu\text{m}^{-1}$ , and since the microchamber curvature is  $C = 0.25 \mu\text{m}^{-1}$ , we extracted a snapback ratio of  $\kappa \approx 0.194/0.25 = 0.78$  (Supplementary Fig. 8b).

Repeating the foregoing analysis with a global, circle fit to the midline yields similar results. In particular, we performed a global fit to the cell by considering the circle joining the head, midpoint, and tail of each

cell, where the midpoint is determined as the point that bisects the length of the cell in the ninth-order polynomial fit. We found that

$$\lambda = 0.0425/\text{frame}, \quad \mu = 0.0877/\text{frame}, \quad (\text{S55})$$

corresponding to a straightening ratio of  $\mu/\lambda = 2.06$ . Supplementary Fig. 8a shows a time series of the curvature as computed with the global fit, which can be compared to that computed with the segmented fit. The average curvature at frame  $t = 1$  was determined again to be  $C(1) = 0.18 \mu\text{m}^{-1}$ , and extrapolating to find the initial curvature yielded  $C(0) = 0.18 \exp(\mu) \approx 0.197 \mu\text{m}^{-1}$ . Since the microchamber curvature is  $C = 0.25$ , the snapback ratio is  $\kappa \approx 0.79$ ; this is nearly identical to the value found with the segmented fit.

**Finite-element simulations with Abaqus FEA.** We used Abaqus FEA to obtain the equilibrium stress profile in the following cases:

1. Cylindrical shell under internal pressure held at one end against a mandrel and subject to a point force at the other end.
2. Closed toroidal section subject to an internal pressure.
3. Closed cylindrical shell with sinusoidally varying elastic modulus subject to an internal pressure.
4. Closed toroidal section composed of an orthotropic material subject to an internal pressure, with the anisotropy specified by engineering constants.

Abaqus input files (.inp format) were created with MATLAB, with shells being discretized uniformly into approximately 10,000 S4R elements. The shells were specified to have elastic modulus 1, Poisson ratio 0.2-0.5, radius 3 units, thickness 0.1 units, and pressures ranging from 0.00001-0.007 units unless otherwise noted. The larger values of pressure correspond to finite strains of the order of  $pr/Y \sim 0.1$ , and estimates of the material properties of *E. coli* suggest that they lie in this regime (Supplementary Table 1). The length was discretized into 300 elements and the circumference was discretized into 32 elements; varying the fineness of this discretization yielded similar results. For closed surfaces, flat endcaps were placed with a thickness of 1000 simulation units; we repeated our simulations for different thicknesses ranging from 0.1-1000 simulation units and found our reported results to be robust to this variation. For case (2), the bending parameter of the torus was varied from  $c = 0.01$  to 0.1. For case (3), 32 different element sets with sinusoidally varying elastic moduli, for which the variational parameter  $d$  ranged from 0.1 to 0.7, were assigned to elements circumferentially. For case (4), a part orientation was defined and the orthotropic material properties were specified with engineering constants. In all cases, the option of geometric nonlinearity was turned on and surface coordinate systems were specified appropriately. For all simulations, we verified that the stress profiles are identical along the bulk of the shell, excluding a small region near the endcaps.

**Discrete simulations of the growth process.** In order to provide numerical evidence for the validity of extending the limits of integration to  $\mp\infty$  in equation (S17), we simulated the growth process with MATLAB for parameter values similar to those in Supplementary Table 1 and assessed whether the straightening rate agreed with equation (S50). We initiated a set of time series describing the pole-to-pole lengths  $L(\theta)$  at discretized angles  $\theta \in [0, 2\pi]$  and nucleated a discrete number ( $\sim 30$ ) of new growth sites. The number of growth sites at each angle differed depending on both the pole-to-pole length and the differential areal strain at that angle, as prescribed by the integrand of equation (S17). We increased  $L(\theta)$  by an amount proportional to the number of growth sites at  $\theta$ . Each growth site was then translocated with an angular velocity  $M$  and randomly removed according to a Poisson process with rate  $1/\tau$ . In the continuum limit, this numerical simulation agrees with the numerical solution of the growth equation, as discussed in the Methods section of the main text. The simulation results, which are shown in Supplementary Fig. 5 and Supplementary Video 11, suggest that:

1. extending the limits of integration to  $\mp\infty$  in equation (S17) is valid as an approximation;
2. after the areal strain profile flips signs, the transient effect due to old growth sites (which were nucleated according to a different areal strain profile) is negligible for the parameter values considered.

**MreB-msfGFP fluorescence analysis methodology.** Cell boundaries were detected from phase contrast microscopy images using the MATLAB-based cell segmentation tool Morphometrics (SimTK) [23]. The cell poles and the cell centerline were identified using the MicrobeTracker package (Supplementary Figs. 9a-b) [28]. The centerline was used for a cell-internal orthogonal coordinate system, with  $X$  the contour length along the centerline. Sample points  $X_i$  were equally spaced along the contour with an interval of 0.5 pixels, and the second coordinates of these points were chosen perpendicular to the centerline.

To measure the bending-induced curvature of the cell body  $C(X)$  rather than local curvature fluctuations on the cell boundaries, we smoothed the  $x$ - and  $y$ -coordinates of the raw, extracted centerline using a Gaussian filter (with a standard deviation of 12.5 pixels) and subsequently calculated the curvature at every smoothed sample point as described. We only considered cells that do not show centerline curvatures with opposite signs, indicative of twisting, and we chose the orientation of the cell poles so that the centerline curvature is positive for every cell. The inside and outside boundaries of the cell are thus always on the left and right sides of the centerline, respectively, when observed along the cell contour.

MreB-msfGFP images were filtered with a 2D Gaussian filter (with a standard deviation of 0.5 pixels) to remove pixel noise. In analyzing MreB intensity ratio and curvature, we only considered the “central region” of the cell, which constitutes 40% of the cell length (Supplementary Fig. 9b). We therefore excluded the cell poles and also the regions that appear as straight during microscopy in two dimensions: this may, presumably, be due to cell twisting upon release from confinement and during recovery. To extract the MreB-msfGFP intensities  $I_{in/out}(X)$  on the inner and outer cell boundaries closest to the centerline point  $X$ , filtered image intensities were linearly interpolated at 5 equally spaced points within a 130 nm-long interval perpendicular to the cell centerline and centered about the inner or outer boundaries. The interpolated intensity values were averaged to yield the MreB intensity values  $I_{in/out}(X)$  on the inner and outer cell boundaries. To ensure that possible discrepancies between the boundaries identified from phase-contrast images and the physical cell boundaries did not lead to artifacts in our measurements, we checked that our analysis yields almost the same average MreB intensity ratio values for intervals as large as 300 nm (Supplementary Fig. 9c-d). MreB-msfGFP intensity values were normalized by the average over all boundary values in the region of interest (Supplementary Fig. 9b) as

$$I(X) = I_{in/out}^{raw}(X) \left( \frac{1}{2N} \sum_i (I_{in}^{raw}(X_i) + I_{out}^{raw}(X_i)) \right)^{-1}, \quad (S56)$$

where  $N$  is the number of points along the centerline region of interest. Average values were obtained by summation over all datapoints  $X_i$  in all cells. The conditional MreB intensity as a function of local centerline curvature,  $\mathcal{I}(C)$ , is the binned average of all normalized boundary intensities associated with a centerline curvature close to  $+C$  (outside boundaries) or  $-C$  (inside boundaries), reflecting the positive and negative curvature of the outer and inner cell edges, respectively.

We verified that our analysis of average curvature and average MreB intensity ratio are robust with respect to changes of the region of interest between 35% and 45% of the cell length (Supplementary Fig. 9c). Furthermore, the curves displaying the MreB intensity ratio as a function of centerline curvature do not depend on the region of interest as long as cell poles are excluded (Supplementary Fig. 9d), consistent with the idea that within experimental conditions MreB intensity ratio is dictated by centerline curvature. Using an independent method of quantifying MreB localization by partitioning the cell in half along the midline and taking the pixel average over the inner and outer bulks, we found that the population average enrichment of the inner bulk drops from 1.07 at 10 mins after release to 1.05 at 30 mins after release and that the distribution becomes markedly shifted to the left (Supplementary Fig. 10a).

Finally, we checked the population-averaged straightening ratio of 60 MreB-msfGRP fusion cells and found that it was  $\approx 1.66$ , similar to that of the wild-type cells ( $\approx 1.8$ ) used in this study (Supplementary Fig. 10b).

## Supplementary References

- [1] Amir, A., Babaeipour, F., McIntosh, D. B., Nelson, D. R. & Jun, S. Bending forces plastically deform growing bacterial cell walls. *Proc. Natl. Acad. Sci. USA* **111**, 5778–5783 (2014).
- [2] Amir, A. & van Teeffelen, S. Getting into shape: How do rod-like bacteria control their geometry? *Syst. Synth. Biol.* **8**, 227–235 (2014).
- [3] van Teeffelen, S. *et al.* The bacterial actin MreB rotates, and rotation depends on cell-wall assembly. *Proc. Natl. Acad. Sci. USA* **108**, 15822–15827 (2011).
- [4] Garner, E. C. *et al.* Coupled, circumferential motions of the cell wall synthesis machinery and MreB filaments in *B. subtilis*. *Science* **333**, 222–225 (2011).
- [5] Domínguez-Escobar, J. *et al.* Processive movement of MreB-associated cell wall biosynthetic complexes in bacteria. *Science* **333**, 225–228 (2011).
- [6] Efrati, E., Sharon, E. & Kupferman, R. The metric description of elasticity in residually stressed soft materials. *Soft Matter* **9**, 8187 (2013).
- [7] Santangelo, C. D. Buckling thin disks and ribbons with non-Euclidean metrics. *EPL* **86**, 34003 (2009).
- [8] Brazier, L. G. On the flexure of thin cylindrical shells and other “thin” sections. *Proc. R. Soc. A* **116**, 104–114 (1927).
- [9] Calladine, C. R. *Theory of Shell Structures* (Cambridge University Press, 1983).
- [10] Jordan, P. F. Stresses and deformations of the thin-walled pressurized torus. *J. Aerospace Sci.* **29**, 213–225 (1962).
- [11] Sanders, J. L. & Liepins, A. A. Toroidal membrane under internal pressure. *AIAA J.* **1**, 2105–2110 (1963).
- [12] Dean, W. R. The distortion of a curved tube due to internal pressure. *Philos. Mag.* **28**, 452–464 (1939).
- [13] Jiang, H. & Sun, S. X. Growth of curved and helical bacterial cells. *Soft Mat.* **8**, 7446 (2012).
- [14] Amir, A. & Nelson, D. R. Dislocation-mediated growth of bacterial cell walls. *Proc. Natl. Acad. Sci. USA* **109**, 9833–9838 (2012).
- [15] Amir, A., Paulose, J. & Nelson, D. R. Theory of interacting dislocations on cylinders. *Phys. Rev. E Stat. Nonlin. Soft Matter Phys.* **87**, 042314 (2013).
- [16] Sliusarenko, O., Cabeen, M. T., Wolgemuth, C. W., Jacobs-Wagner, C. & Emonet, T. Processivity of peptidoglycan synthesis provides a built-in mechanism for the robustness of straight-rod cell morphology. *Proc. Natl. Acad. Sci. USA* **107**, 10086–10091 (2010).
- [17] Yao, X., Jericho, M., Pink, D. & Beveridge, T. Thickness and elasticity of Gram-negative murein sacculi measured by atomic force microscopy. *J. Bacteriol.* **181**, 6865–6875 (1999).
- [18] Deng, Y., Sun, M. & Shaevitz, J. W. Direct measurement of cell wall stress stiffening and turgor pressure in live bacterial cells. *Phys. Rev. Lett.* **107**, 158101 (2011).
- [19] Typas, A., Banzhaf, M., Gross, C. A. & Vollmer, W. From the regulation of peptidoglycan synthesis to bacterial growth and morphology. *Nat. Rev. Microbiol.* **10**, 123–136 (2012).
- [20] Vollmer, W., Joris, B., Charlier, P. & Foster, S. Bacterial peptidoglycan (murein) hydrolases. *FEMS Microbiol. Rev.* **32**, 259–286 (2008).
- [21] Harris, L. K., Dye, N. A. & Theriot, J. A. A *Caulobacter* MreB mutant with irregular cell shape exhibits compensatory widening to maintain a preferred surface area to volume ratio. *Mol. Microbiol.* **94**, 988–1005 (2014).

- [22] Kim, S. Y., Gitai, Z., Kinkhabwala, A., Shapiro, L. & Moerner, W. E. Single molecules of the bacterial actin MreN undergo directed treadmilling motion in *Caulobacter crescentus*. *Proc. Natl. Acad. Sci. USA* **103**, 10929–10934 (2006).
- [23] Ursell, T. S. *et al.* Rod-like bacterial shape is maintained by feedback between cell curvature and cytoskeletal localization. *Proc. Natl. Acad. Sci. USA* **111**, 1025–1034 (2014).
- [24] Rojas, E., Theriot, J. A. & Huang, K. C. Response of *Escherichia coli* growth rate to osmotic shock. *Proc. Natl. Acad. Sci. USA* **111**, 7807–7812 (2014).
- [25] Pilizota, T. & Shaevitz, J. W. Fast, multiphase volume adaptation to hyperosmotic shock by *Escherichia coli*. *PLOS ONE* **7**, e35205 (2012).
- [26] Tuson, H. H. *et al.* Measuring the stiffness of bacterial cells from growth rates in hydrogels of tunable elasticity. *Mol. Microbiol.* **85**, 874–891 (2012).
- [27] Stewart, E. J., Madden, R., Paul, G. & Taddei, F. Aging and death in an organism that reproduces by morphologically symmetric division. *PLoS Biol.* **3**, e45 (2005).
- [28] Sliusarenko, O., Heinritz, J., Emonet, T. & Jacobs-Wagner, C. High-throughput, subpixel precision analysis of bacterial morphogenesis and intracellular spatio-temporal dynamics. *Mol. Microbiol.* **80**, 612–627 (2011).
- [29] Huang, K. C., Mukhopadhyay, R., Wen, B., Gitai, Z. & Wingreen, N. S. Cell shape and cell-wall organization in gram-negative bacteria. *Proc. Natl. Acad. Sci. USA* **105**, 19282–19287 (2008).
- [30] Vollmer, W., Blanot, D. & de Pedro, M. A. Peptidoglycan structure and architecture. *FEMS Microbiol. Rev.* **32**, 149–167 (2008).
- [31] Simmons, G. & Wang, H. *Single crystal elastic constants and calculated aggregate properties: a handbook* (MIT Press, 1971).
- [32] Volkmer, B. & Heinemann, M. Condition-dependent cell volume and concentration of *Escherichia coli* to facilitate data conversion for systems biology modeling. *PLoS ONE* **6**, e23126 (2011).
- [33] Bakshi, S., Siryaporn, A., Goulian, M. & Weisshaar, J. C. Superresolution imaging of ribosomes and RNA polymerase in live *Escherichia coli* cells. *Mol. Microbiol.* **85**, 21–38 (2012).
- [34] Koch, A. L. The surface stress theory for the case of *Escherichia coli*: the paradoxes of Gram-negative growth. *Res. Microbiol.* **141**, 119–130 (1990).
- [35] Cayley, D. S., Guttman, H. J. & Record, M. T. Biophysical characterization of changes in amounts and activity of *Escherichia coli* cell and compartment water and turgor pressure in response to osmotic stress. *Biophys. J.* **78**, 1748–1764 (2000).
- [36] Dmitriev, B. A. *et al.* Tertiary structure of bacterial murein: the scaffold model. *J. Bacteriol.* **185**, 3458–3468 (2003).

## Supplementary Tables

Quantity	Symbol	Value	Source
Material parameters			
Cell wall elastic modulus (3D)	$E$	20-30 MPa	[1, 17, 18]
Cell wall thickness	$h$	3 nm	[29, 30]
Cell wall elastic modulus (2D)	$Y$	0.06-0.09 N/m	$Y = Eh$
Cell wall Poisson ratio	$\nu$	0.16-0.30	[17, 31]
Cell radius	$r$	0.5 $\mu\text{m}$	experiment, [32, 33]
Turgor pressure	$p$	0.3-2 atm	[18, 34, 35]
Dimensionless pressure	$\eta$	0.16-1.11	$\eta = pr/Y$
MreB persistence time	$\tau$	5 min	[23]
MreB spot velocity	$v$	5 nm/s	[3, 21, 22]
MreB angular velocity	$M$	0.01 rad/s	$M = v/r$
MreB processivity	$M\tau$	3 rad	extracted
Straightening parameters			
Microchamber radius	$R_{\text{curv}}$	4 $\mu\text{m}$	experiment
Microchamber bending parameter	$B^0$	0.125	$B^0 = r/R_{\text{curv}}$
Snapback ratio	$\kappa$	$0.78 \pm 0.09$	extracted
Steady-state differential growth	$c^0$	$0.098 \pm 0.011$	$\kappa = c^0/B^0$
Peptidoglycan insertion width	$L_0$	1.1 nm	[36]
Peptidoglycan turnover rate	$f_t$	0.40	[19, 20]
Constant net growth initiation rate	$k$	$13 \mu\text{m}^{-2} \cdot \text{min}^{-1}$	$k = \frac{\lambda(1+\lambda\tau)}{M\tau L_0 r}$
Constant new growth initiation rate	$k_{\text{new}}$	$21 \mu\text{m}^{-2} \cdot \text{min}^{-1}$	$k_{\text{new}} = \frac{k}{1-f_t}$
Constant degradation rate	$k_{\text{deg}}$	$8 \mu\text{m}^{-2} \cdot \text{min}^{-1}$	$k_{\text{deg}} = \frac{f_t k}{1-f_t}$
Areal strain-growth coupling parameter	$\alpha$	$200-400 \mu\text{m}^{-2} \cdot \text{min}^{-1}$	$\alpha \approx \frac{\kappa M \lambda \tau}{L_0 r \xi_0 (1-\kappa)}$
Doubling time	$t_d$	33 min	extracted
Growth rate	$\lambda$	0.0208-0.0213 $\text{min}^{-1}$	extracted
Straightening rate	$\mu$	0.0376-0.0439 $\text{min}^{-1}$	extracted

Supplementary Table 1: Variables used (or calculated) in the paper and their numerical values.

		Phase 1	Phase 2	
Measurement	Temperature	after 2 doubling times	5 min after extraction	30 min after extraction
Curvature ( $\mu\text{m}^{-1}$ )	30°C	0.26	0.24	no data
	37°C	0.271 SD = 0.018	0.25 SD = 0.03	0.216 SD = 0.066
MreB intensity ratio between inner and outer edges	30°C	1.05	1.16	no data
	37°C	1.07 SD = 0.019	1.103 SD = 0.02	1.052 SD = 0.002

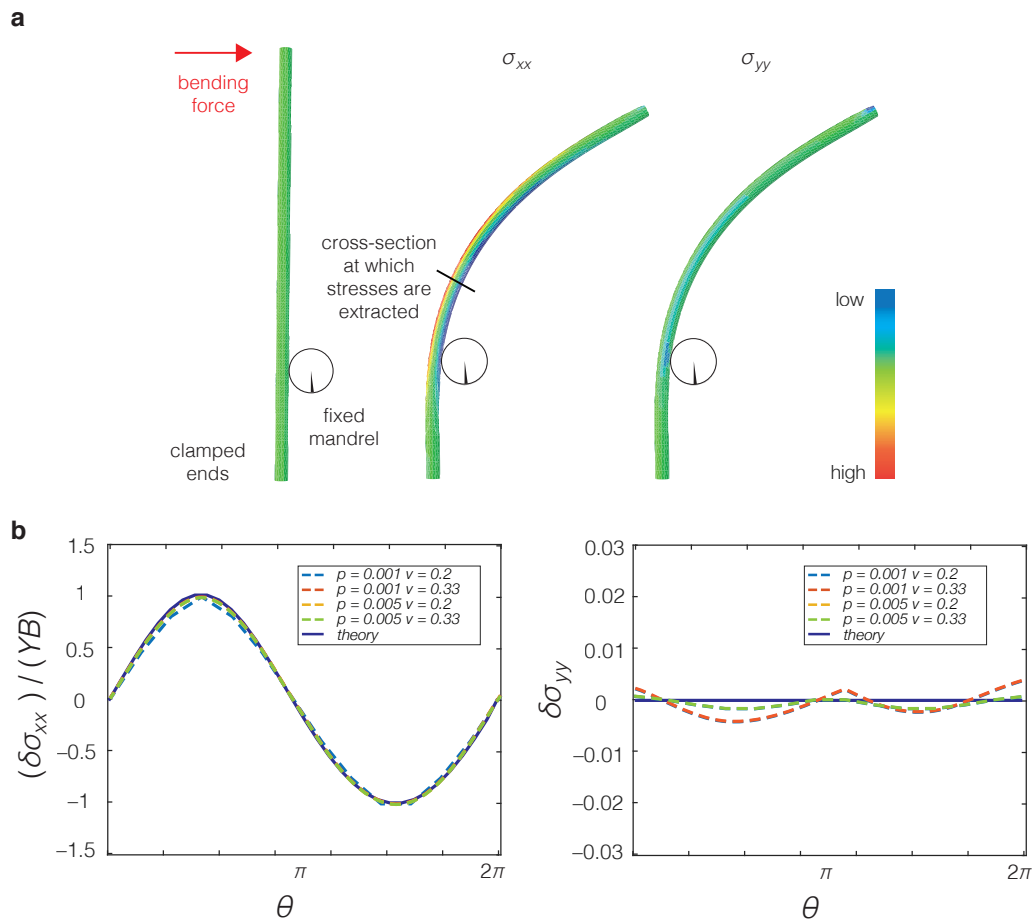
Supplementary Table 2: Mean cell centerline curvature and MreB intensity ratios of the MreB-msfGFP fusion strain at different temperatures inside confinement, 5 min after extraction, and 30 min after recovery. The standard deviation values (SD) are acquired from the repetitions of the same experiment. Measurements were obtained for 17 cells in Phase 1 and 20 cells 5 min after release at 30°C, and 119 cells in Phase 1, 132 cells 5 min after release, and 32 cells 30 min after release at 37°C.

## Supplementary Videos

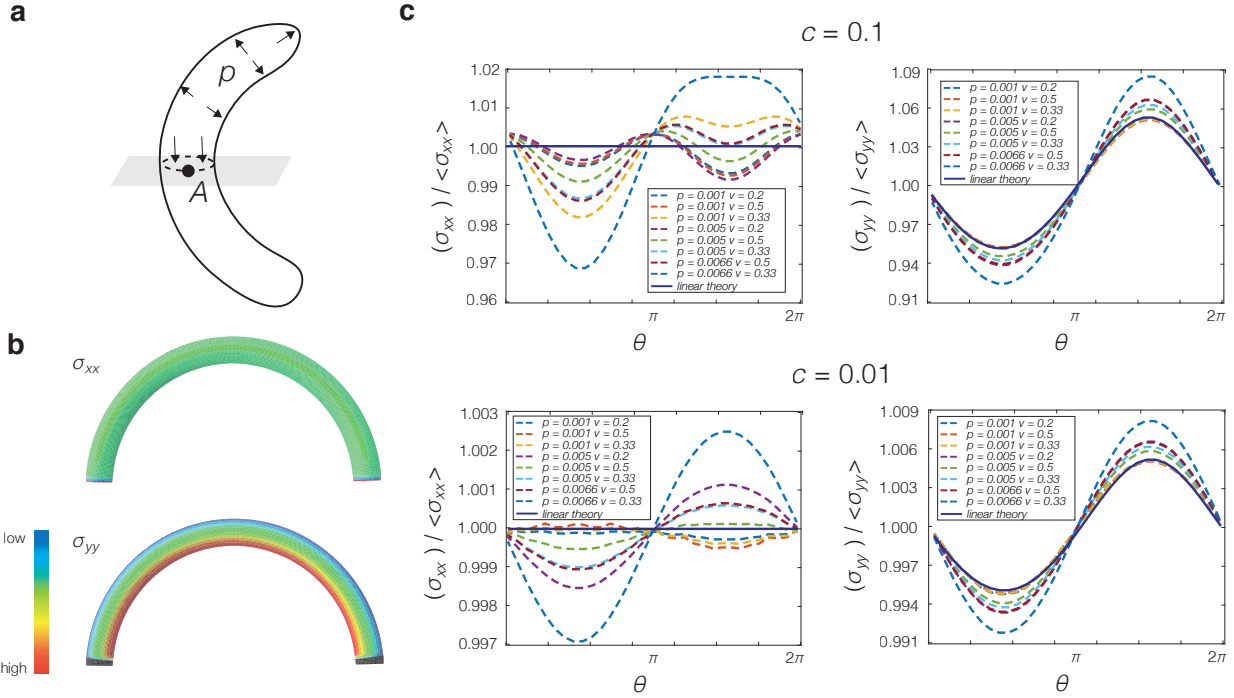
Supplementary Videos 1–10: **Straightening dynamics of single *E. coli* cells.** Supplementary Videos 1 to 10 show individual, filamentous *E. coli* cells recovering their native rod shapes as they grow after release from toroidal microchambers. The time between frames is 2 minutes, the time lapses cover a period of about 40 minutes, and the field of view is approximately 40  $\mu\text{m}$  wide.

Supplementary Video 11: **Numerical simulation of the growth process.** Supplementary Video 11 shows numerical simulations in (1) the case of zero processivity; (2) the case of infinite processivity; and (3) the case of a self-consistent areal-strain coupling that results in a constant differential growth in Phase 1 and straightening in Phase 2. The simulation methodology is detailed in the Supplementary Methods.

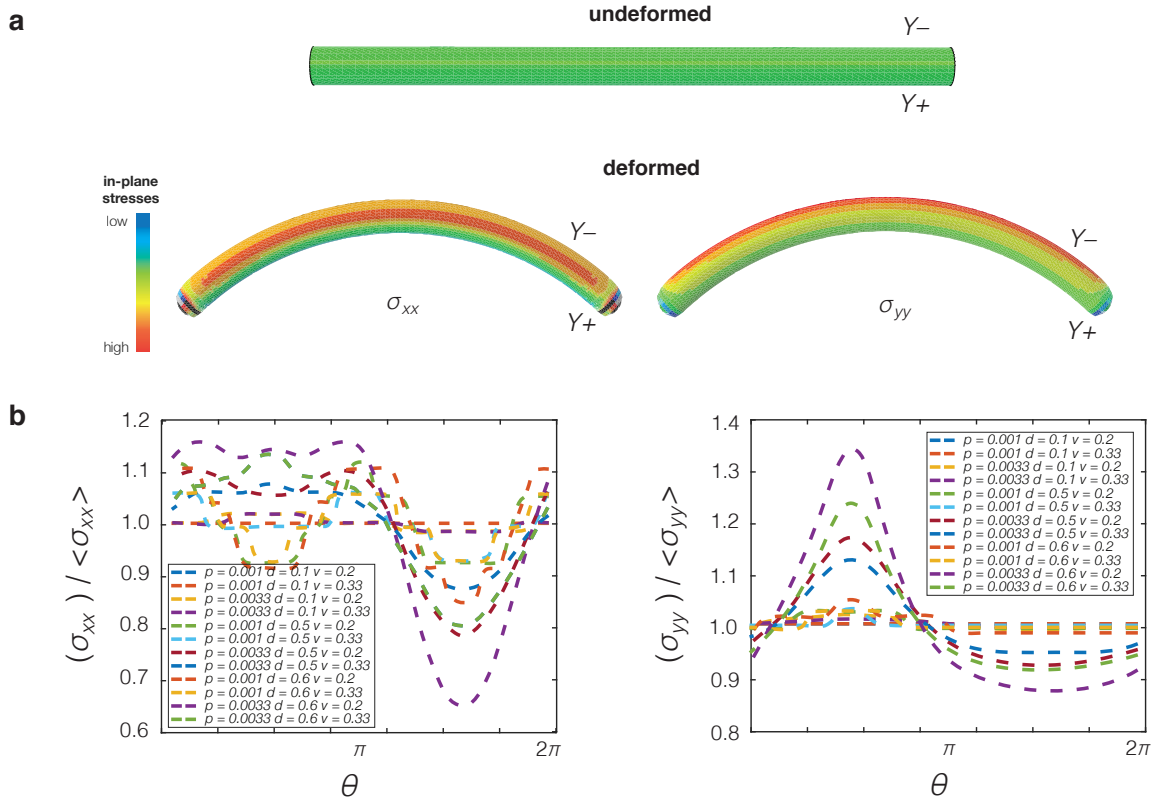
## Supplementary Figures



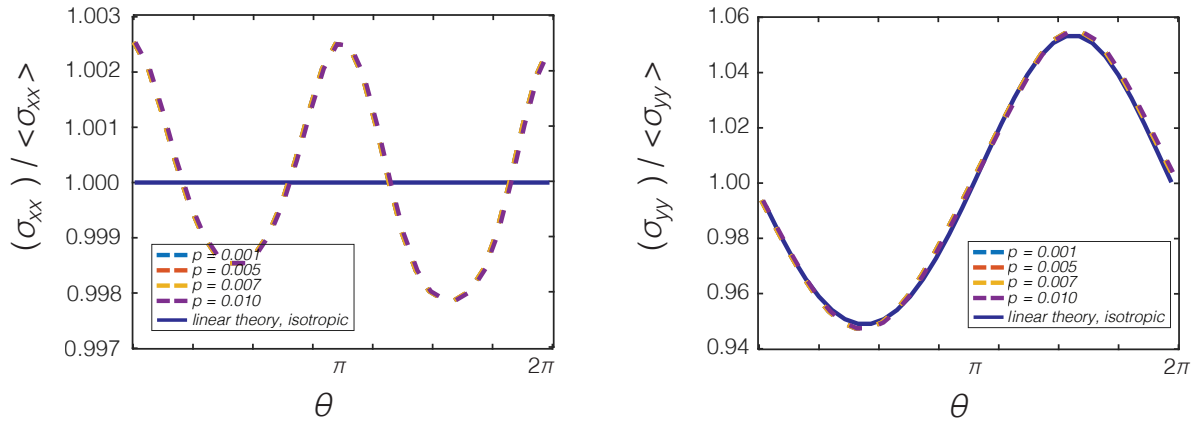
Supplementary Figure 1: **Stress profiles of pressurized cylindrical shells subject to bending moments.** **a**, Abaqus FEA simulations of a pressurized cylindrical shell subjected to a bending force against a fixed mandrel. **b**, Plots of the stress resultants for typical cross-sections indicated in **a** for varying values of  $p$  and  $\nu$ . The remaining simulation parameters are discussed in the Supplementary Methods. The theoretical prediction agrees with the simulated stress profiles. We interpret the small variations in the simulated  $\sigma_{yy}$  profiles to arise from a small eccentricity induced by bending, which is quantitatively consistent with equation (S8) (not shown).



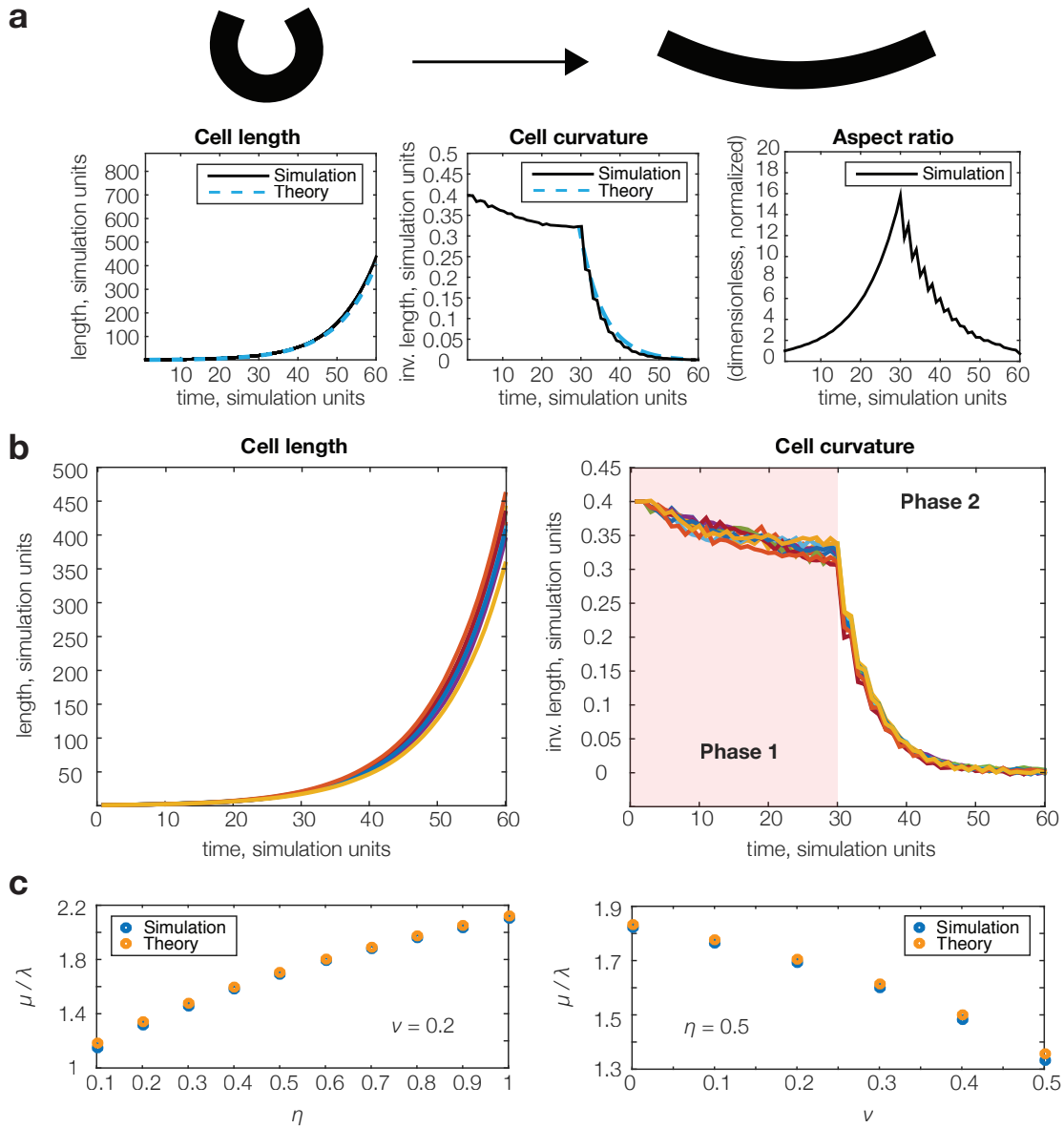
Supplementary Figure 2: **Stress profiles of closed toroidal shells subject to internal pressure.** **a**, A toroidal section with a circular cross-section at equilibrium cannot have a nonvanishing torque due to pressure. **b**, Abaqus FEA simulations for the equilibrium of an initially circular toroidal segment subject to internal pressure, where the axial and circumferential stress resultants  $\sigma_{xx}$  and  $\sigma_{yy}$  are displayed. Here  $pr/Y = 0.03$ ,  $\nu = 0.2$ , and the differential growth parameter is  $c = 0.1$ . The remaining simulation parameters are discussed in the Supplementary Methods. **c**, Plots of the normalized stress resultants  $\sigma_{xx}/\langle\sigma_{xx}\rangle$  and  $\sigma_{yy}/\langle\sigma_{yy}\rangle$  as functions of the azimuthal coordinate  $\theta$ , for  $c = 0.01$  and  $c = 0.1$ . The remaining simulation parameters are again discussed in the Supplementary Methods. A variational component in  $\sigma_{xx}$ , which is small compared to the variational component in  $\sigma_{yy}$ , arises for large strains on the order of 0.1, and is generally non-sinusoidal. Nevertheless, the stress resultants remain well-approximated by the linear theory result for a pressurized torus of circular cross-section.



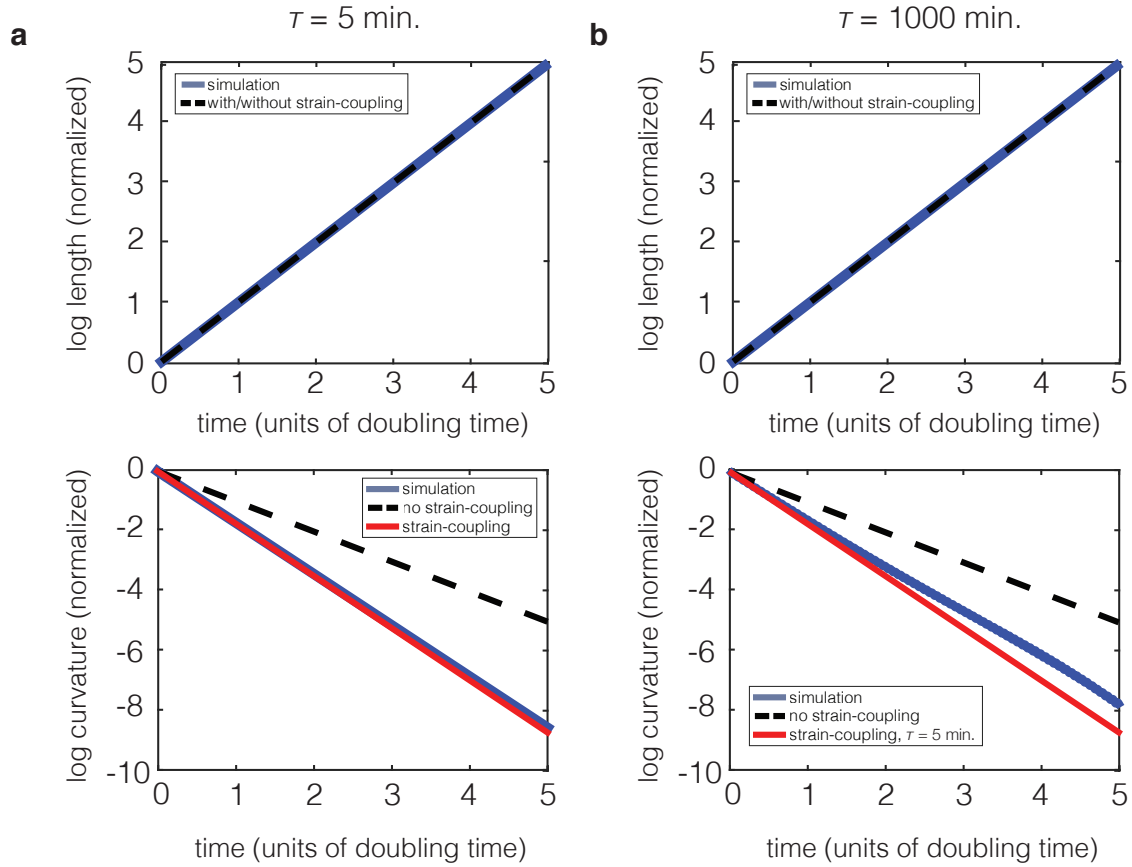
Supplementary Figure 3: **Finite-element simulations of shells with varying elastic moduli.** **a**, Abaqus FEA simulations of a capped, pressurized cylindrical shell with a sinusoidally varying elastic modulus of the form  $Y(\theta) = Y(1 + d \sin \theta)$ . Here  $pr/Y \approx 0.1$ ,  $\nu = 0.2$ , and the variational parameter  $d = 0.6$ . The remaining simulation parameters are detailed in the Supplementary Methods. Note that, in the deformed state, both  $\sigma_{xx}$  and  $\sigma_{yy}$  are larger on the outer edge but generally exhibit complex behavior. **b**, A plot of the normalized stress resultants  $\sigma_{xx}/\langle\sigma_{xx}\rangle$  and  $\sigma_{yy}/\langle\sigma_{yy}\rangle$  for a range of  $p$ ,  $d$ , and  $\nu$ , with the remaining simulation parameters as discussed in the Supplementary Methods.



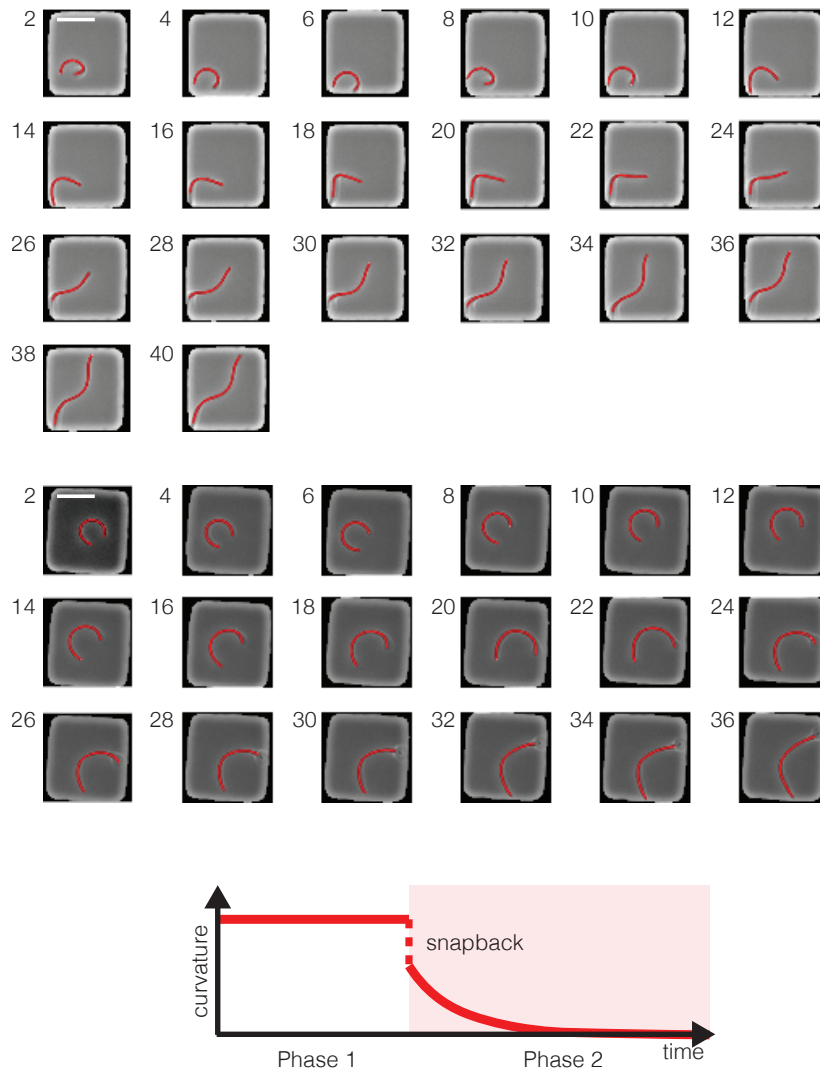
Supplementary Figure 4: **Finite-element simulations of shells with anisotropic material properties.** A plot of the normalized stress resultants  $\sigma_{xx}/\langle\sigma_{xx}\rangle$  and  $\sigma_{yy}/\langle\sigma_{yy}\rangle$  corresponding to a capped, pressurized toroidal section for varying  $p$  and orthotropic material properties specified by engineering constants. Here  $r = 3$ ,  $h = 0.1$ , the axial and circumferential elastic moduli  $E_x = E_z = 1$  and  $E_y = 2$ , the Poisson ratios  $\nu_{xy} = \nu_{xz} = \nu_{yz} = 0.33$ , and the shear moduli  $G_{xy} = G_{xz} = G_{yz} = 1$ .



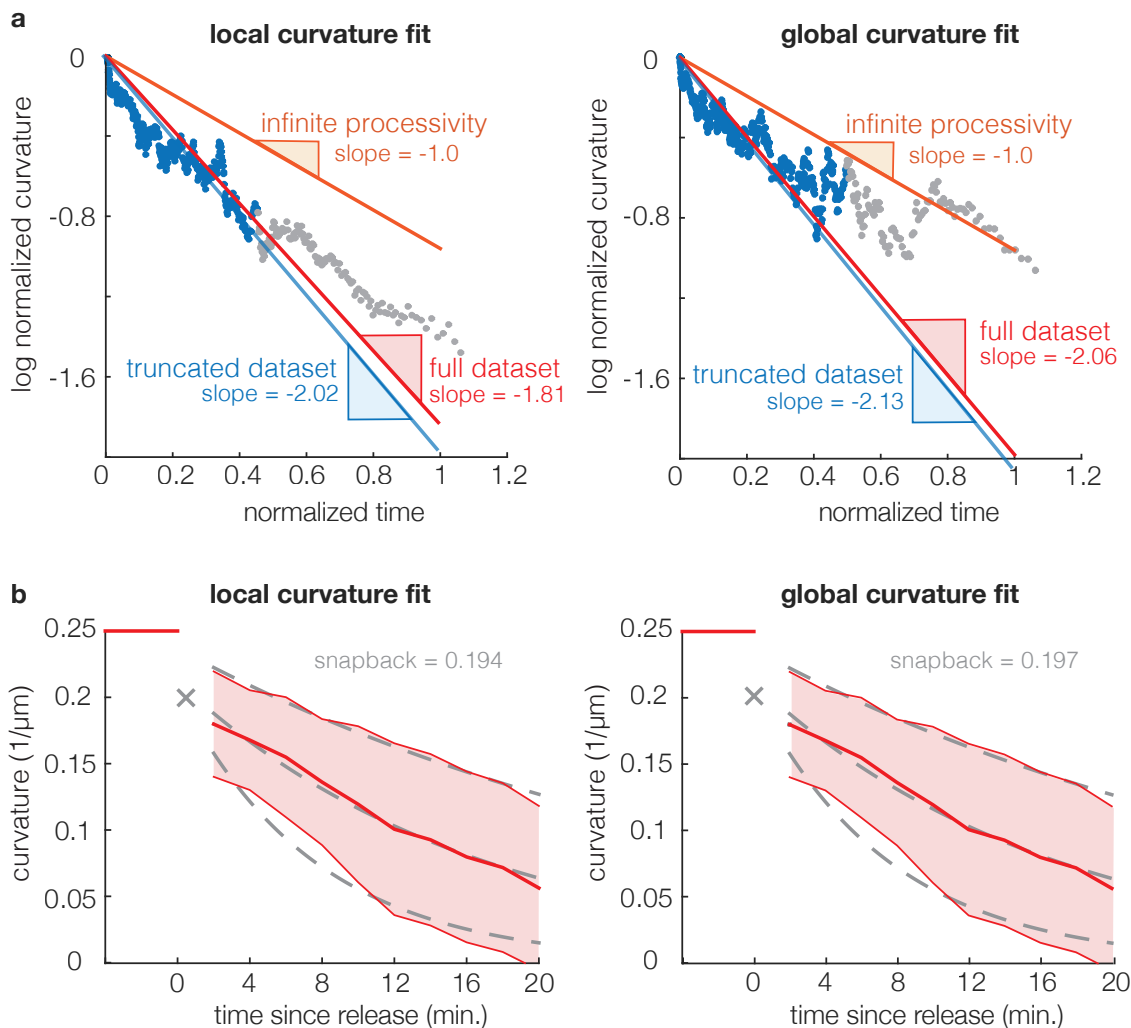
Supplementary Figure 5: **Numerical simulation of the growth process.** **a**, Simulation results for parameter values faithful to *E. coli*, as summarized in Supplementary Table 1 and the Supplementary Methods, except that we have set  $c^0 = 0.35$  to emphasize the curvature decay in the associated Supplementary Video 11. By coupling growth to areal strains, the cell grows at a steady-state value of the differential growth parameter for  $t < 30$  and straightens for  $t > 30$ . See Supplementary Video 11 for an animation of the growth process. **b**, Different simulations of **a**. Although the discrete nature of the initiation and growth process may introduce variations in cell length and curvature, these simulations suggest a negligible transient effect due to old growth sites once the areal strain profile has flipped. **c**, Average simulated straightening rates with the same parameters as **a**, except  $\eta$  and  $\nu$  are varied. The simulation results agree with the theoretical prediction for a range of  $\eta$  and  $\nu$ .



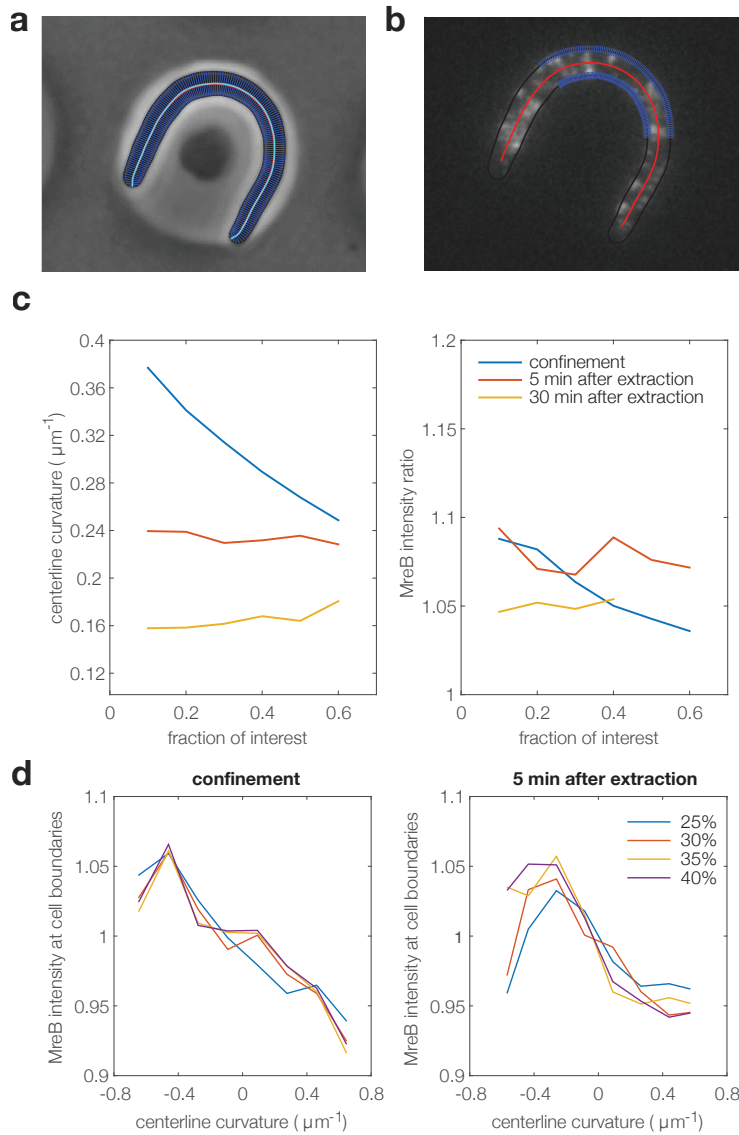
Supplementary Figure 6: **Numerical solutions of the growth equation.** **a**, A numerical solution of equation (S23) in the regime  $\tau : M\tau \gg 1 \gg \mu\tau > \lambda\tau$ , where all parameters are set to values in the ranges specified by Supplementary Table 1. The length along the midline of the cell grows exponentially with rate  $\lambda$ . As expected, the curvature decays exponentially with rate  $\lambda$  in the case of infinite processivity with no areal strain-coupling (dashed black line), but faster in the case where there is strain-coupling (solid blue line). The solid red line is the curve  $-\mu t$ , with  $\mu$  given by equation (S50), which agrees with the numerical result. **b**, A numerical solution of equation (S23) in the regime  $\tau : M\tau \gg \mu\tau > \lambda\tau > 1$ , where  $M = 0.6$  rad/min and  $\tau = 1000$  min. The remaining parameter values are set according to Supplementary Table 1. This corresponds to the case where MreB may persist longer than the doubling time of the cell, as discussed in Supplementary Note 2. Although small amplitude oscillations appear (inset), the curvature decays at an average rate that is higher than the prediction of infinite processivity, but lower than the case of an intermediate processivity with strain-coupling (a).



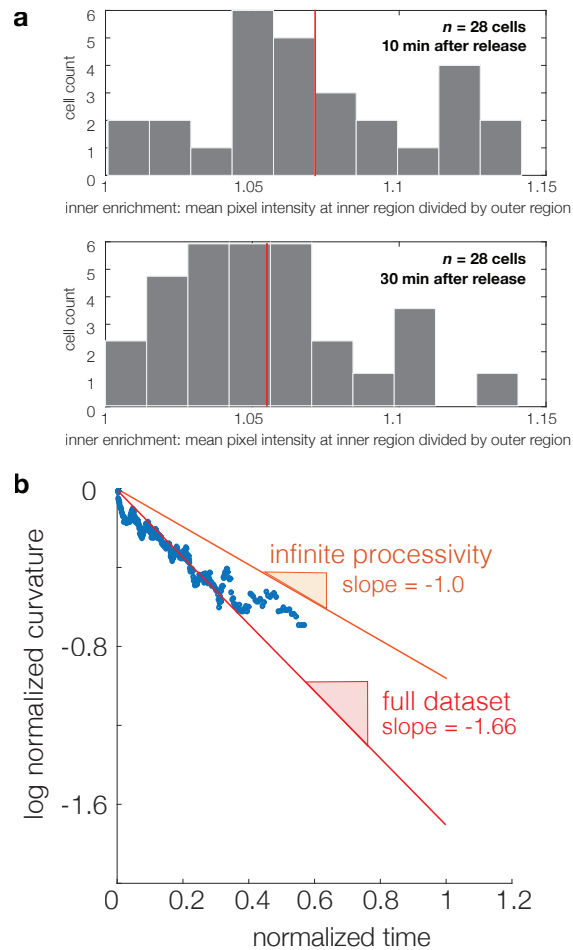
Supplementary Figure 7: *CurvatureTracker* results. Two examples of single-cell straightening events, corresponding to an exponential decay of curvature, tracked by *CurvatureTracker* out of a sample size of 60. Red curves indicate ninth-degree parametric polynomial fits and are overlaid on top of the cell. The time between frames is 2 minutes, as indicated on the upper-left corner of each frame, and the field of view is approximately 40  $\mu\text{m}$  wide. These image sequences correspond to the straightening behavior observed in Phase 2 of our experiments (bottom). Scale bars denote 20  $\mu\text{m}$ .



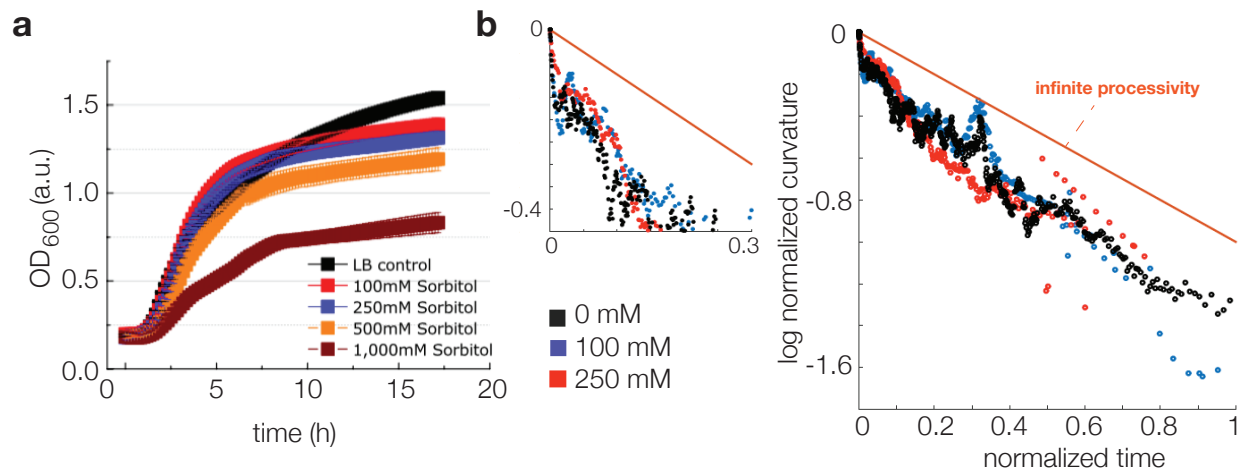
Supplementary Figure 8: **Image analysis results.** **a**, Aggregated straightening data from all 60 cells, where both a local, segmented fit (left) and a global fit (right) to the cell curvature were used. Unlike Fig. 4c of the main text, a moving average filter was not applied. The time is plotted in units of  $1/\lambda$ , corresponding to the doubling time of the cell divided by  $\ln(2)$ . The log normalized curvature is defined as  $\ln(C(t)/C(t = 2 \text{ min}))$ , where  $C(t)$  is the curvature of the cell at time  $t$ . The gray data points were discarded in considering a truncated fit, as discussed in the Supplementary Methods; because the blue data points are significantly denser, the straightening rates of the truncated datasets lie within only 5% of the full dataset values for both fits. **b**, Plots of average cell curvature against time for both fits. Extrapolating the population-averaged cell curvature (thick red curve) via an exponential fit to  $t = 0$  allows us to infer the snapback ratios. Shaded areas denote values within one standard deviation of the population means. The gray dashed lines denote exponential fits to values which are one standard deviation away from the population average.



Supplementary Figure 9: **MreB-msfGFP fluorescence analysis methodology and sensitivity analysis.** **a**, For MreB-msfGFP measurements, cell contours are obtained from phase contrast images and an cell-internal coordinate system is developed based on the cell centerline (cell boundaries in black, smooth centerline in red, raw centerline in cyan, lines perpendicular to raw centerline in blue). **b**, The MreB-msfGFP signal as a function of contour length  $I_{in/out}(X)$  is obtained by linear interpolation and averaging along an interval of points perpendicular to the cell boundaries along the central 40% of the cell (central region is shown in light blue together with cell boundaries and smooth centerline). **c**, Average cell curvature is robust with respect to changes of the cellular regions of interest considered for analysis both after extraction and during recovery. Inside the microchambers, the curvature and MreB intensity ratio drop as a function of the fraction of total cell length considered, consistent with the observation that the ends of cells are often straighter than the central region. Each curve in **c** and **d** was generated by measurements from between 20-40 cells from at least two replicate experiments, as detailed in the Methods section of the main text. **d**, MreB intensity ratio as a function of local curvature is unaffected by the size of the region of interest considered for analysis in microchambers, after extraction, and during recovery. Negative and positive curvatures correspond to inner and outer edges, respectively.



Supplementary Figure 10: **Checking the MreB-msfGFP fluorescence analysis.** **a**, Distributions of the inner MreB enrichment using a simple bulk pixel averaging method, at two different times in Phase 2, which are representative of three replicate experiments. The red line denotes the mean. **b**, Population-averaged straightening statistics of the MreB-msfGFP fusion, for a local curvature fit on 60 cells as discussed in the Supplementary Methods. We find a straightening ratio  $\langle\mu\rangle/\langle\lambda\rangle \approx 1.7$ , approximately that of the wild-type strain ( $\langle\mu\rangle/\langle\lambda\rangle \approx 1.8$ ) used in this study (Fig. 4c of the main text).



Supplementary Figure 11: **Effect of hyperosmotic shock on straightening.** **a**, Growth curves of *E. coli* bulk culture subjected to varying degrees of hyperosmotic shock, which are representative of two independent measurements and three repetitions each. **b**, A straightening plot of the hyperosmotically shocked cells for a local curvature fit (60 cells for 0 mM, 22 cells for 100 mM and 27 cells for 250 mM), corresponding to Fig. 4c in the main text.